Oil & Natural Gas Technology

DOE Award No.: DE-NT0005668

Final Report

October 1 2008 to March 31, 2012

Gas Hydrate Characterization in the GoM using Marine EM Methods

Submitted by:
Scripps Institution of Oceanography
University of California San Diego
La Jolla, CA 92093-0225

Principal Investigator: Steven Constable

March 31, 2012

NETL

Office of Fossil Energy

TABLE OF CONTENTS

EXECUTIVE SUMMARY

In spite of the importance of gas hydrate as a low-carbon fuel, a possible contributor to rapid climate change, and a significant natural hazard, our current understanding about the amount and distribution of submarine gas hydrate is somewhat poor; estimates of total volume vary by at least an order of magnitude, and commercially useful concentrations of hydrate have remained an elusive target. This is largely because conventional geophysical tools have intrinsic limitations in their ability to quantitatively image hydrate. It has long been known from well logs that gas hydrate is resistive compared to the host sediments, and electrical and electromagnetic methods have been proposed and occasionally used to image hydrates. This project seeks to expand our capabilities to use electromagnetic methods to explore for gas hydrate in the marine environment.

An important basic science aspect of our work was to quantify the resistivity of pure gas hydrate as a function of temperature at seafloor pressures. We designed, constructed, and tested a high-pressure cell in which hydrate could be synthesized and then subjected to electrical conductivity measurements. Impedance spectroscopy at frequencies between 20 Hz and 2 MHz was used to separate the effect of the blocking electrodes from the intrinsic conductivity of the hydrate. We obtained very reproducible results that showed that pure methane hydrate was several times more resistive than the water ice that seeded the synthesis, 20,000 Ωm at 0°C, and that the activation energy is 30.6 kJ/mol over the temperature range of -15 to 15°C. Adding silica sand to the hydrate, however, showed that the addition of the extra phase caused the conductivity of the assemblage to increase in a counter-intuitive way. The fact that the increased conductivity collapsed after a percolation threshold was reached, and that the addition of glass beads does not produce a similar increase in conductivity, together suggest that while the surface of the gas hydrate grains are not intrinsically conductive, the presence of sand does increase their conductivity.

In the field component of this project, we carried out an 18-day cruise on the R.V. Roger Revelle in the Gulf of Mexico from 7th–26th October 2008 to collect controlled-source electromagnetic (CSEM) data over four hydrate prospects; blocks AC 818, WR 313, GC 955, and MC 118. During these surveys we deployed 30 ocean bottom electromagnetic (OBEM) recorders a total of 94 times at four survey areas and towed the Scripps Undersea Electromagnetic Source Instrument (SUESI) a total of 103 hours. SUESI transmission was 200 A on a 50 m dipole antenna at heights of 70–100 m above the seafloor. We also towed a neutrally buoyant 3-axis electric field recorder behind the SUESI antenna at a constant offset of 300 m. The use of a towed receiver that is "flown" above the seafloor allowed us to operate in areas where seafloor infrastructure such as well-heads, pipelines, and installed scientific equipment existed.

We reduced the data to apparent resistivity psuedosections. The most compelling results come from the hydrate observatory at MC 118, where a localized resistivity anomaly is clearly identified under the southeast crater in an otherwise uniform 1 Ωm background. The data from MC 118 also show that authigenic carbonate does not necessarily express itself as a confounding resistor, as was feared at the start of this project. While the results from the other prospects are much more complicated, the data are well correlated with known geology, and line to line agreement is good. Although these data are not amenable to 1D inversion as was initially hoped, we expect to use a newly developed 2D CSEM inversion code to continue to get useful information from this rich data set.

A number of oil companies and contractor companies supported this work, which resulted in continued funding to further develop and commercialize the towed receiver system pioneered in this study.

1. INTRODUCTION

Clathrate hydrates of natural gas (gas hydrates) are compounds with an ice-like crystalline framework that encages guest gas molecules, most commonly methane. Methane hydrates require cool temperatures, high pressures, and methane in excess of solubility to form, and are found in both marine and permafrost regions worldwide.

Natural gas hydrate is important for a number of reasons:

1. Methane stored in concentrated form in gas hydrates on continental margins and in Arctic permafrost represents a significant source of clean, low-carbon energy.

2. Much naturally occurring hydrate exists at the edge of thermodynamic stability, and as such represents an environmental hazard that threatens release of a potent greenhouse gas. Perturbations in the stability conditions of hydrate may have caused catastrophic release of methane and contributed to past climate change. A more significant contribution to future climate change may come from the chronic decomposition of hydrate, currently taking place in Arctic regions.

3. Gas hydrate poses a more local and immediate threat associated with potential hazards to drilling and offshore slope stability. Hydrate instability has been associated with some of the largest marine landslides documented in the geologic record, which in the future may threaten infrastructure and coastal regions. The threat to drilling and production will become a more significant problem as exploration moves into deeper water and more expanded thermodynamic stability conditions for hydrate.

4. Finally, there has been some recent discussion of an emerging concept to utilize the hydrate cage-like structure to sequester carbon dioxide in the form of CO_2 hydrate. The generation of CO_2 hydrate in the shallow section may form a natural barrier to the undesirable release of carbon dioxide which has been injected as a gravitationally stable fluid into sediments deep enough to be warm and below the hydrate stability field. It will be undoubtedly necessary to develop long-term and non-invasive techniques to monitor hydrate formation during ocean carbon sequestration.

Methane hydrates occur in vast quantities – an estimate of 10,000 Gt (or 21 x 10^{15} m³) of methane is the highly cited "concensus value". However, the global hydrate estimate changes as a result of continued efforts at direct and indirect observation and by the addition of more complex global models, and even recent estimates of hydrate volume span nearly two orders of magnitude. Part of the reason for this is that current geophysical surveying methods for identifying hydrates, such as seismic methods and well logging/coring, are limited. Traditionally, seismic methods to detect hydrate used the bottom simulating reflector (BSR), which runs parallel to the sea floor and often cross-cuts sedimentary structures. The BSR tracks the phase change of solid hydrate (above) and free gas (below) which is controlled by the intersection of the hydrate stability field with the local geothermal gradient. However, the strong seismic signature associated with traces of free gas at the BSR is almost completely independent of the amount of hydrate higher in the section. Thus, hydrates are known to occur in the Gulf of Mexico without a seismic BSR, and many boreholes drilled into well-developed BSRs intersect only traces of hydrate. Seismic blanking and seismic bright spots may be a better indication of hydrate in the section, but reveal little about the thickness and concentration of the material. Quantifying the volume fraction of hydrate in sediments is possible with careful processing and inversion of seismic data, but this approach is far from routine, and the relationship between seismic velocity (or attenuation) and hydrate concentration is complicated. Well logging or coring is expensive, invasive, and provides only a point measurement for the direct presence of hydrate; regional distributions of hydrate are impossible to estimate with this technique alone.

Electromagnetic methods, on the other hand, can be sensitive to the concentration and geometric distribution of hydrate. Resistivity measurements made during well logging indicate that regions containing hydrate are significantly more resistive when compared to water saturated zones. Although the bulk resistivity of a hydrate/sediment system can be lower than localized measurements from well logs, resistivity does provide a suitable EM signal for the detection and quantification of hydrates, allowing the estimation of hydrate volume fraction undisturbed by drilling. However, the use of marine EM techniques to characterize hydrate is in its infancy, and field trials carried out to date are limited in scope and sophistication. Moreover, the EM studies lack the key petrophysical relations (derived from laboratory

studies) to relate conductivity to quantitative estimates of hydrate volume in the surveyed regions.

In the work reported here we begin to address these problems by (a) collecting a number of data sets over different sites in the Gulf of Mexico using a combination of fixed offset and variable offset CSEM sounding along with (b) carefully controlled laboratory measurements of natural gas hydrate conductivity.

2. LABORATORY CONDUCTIVITY MEASUREMENTS ON METHANE HYDRATE

Although well logs from both permafrost and marine environments show that the resistivity of hydrate is higher than that of surrounding sediments, this physical property has been largely ignored in laboratory studies. Many laboratory studies concentrate on tetrahydrofuran (THF) hydrate which has a more manageable stability field. Until now most authors have simply assumed that hydrate is resistive compared with the surrounding sediment. That is a good assumption for Archie's law or lower bound models, in which the conductive phase dominates the bulk conductivity, but it is not a good assumption for hydrate occurring as veins or as massive hydrate, where the resistive phase dominates bulk conductivity. In the work described below we designed and built an electrical conductivity cell suitable for measurements on methane hydrate, and made the first quantitative measurements of methane hydrate conductivity under representative temperatures and pressures.
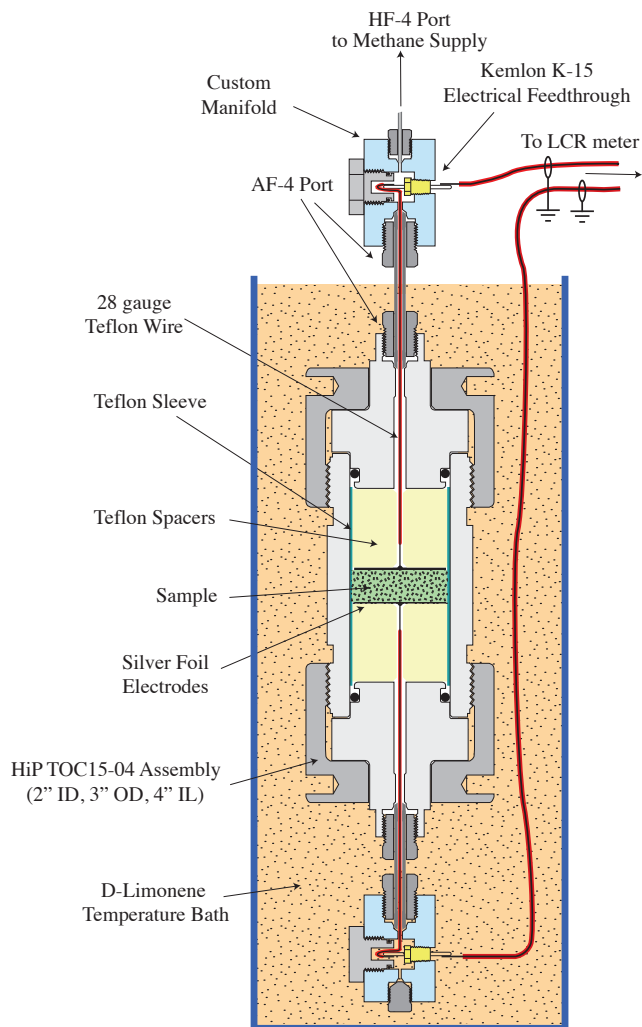

Figure 1. Electrical conductivity cell used to synthesize and simultaneously measure electrical conductivity of gas hydrate. It is built around a commercially available pressure vessel manufactured by High Pressure Equipment Company with the addition of custom high pressure manifolds that allow both methane gas and an electrical feed-though to enter the single port on the vessel's end-caps. The Teflon spacers allow for various sample sizes to be accommodated.

We built an electrical conductivity cell around a commercially available pressure vessel (Figure 1) which allows us to synthesize hydrate *in situ* from ice or ice/sediment mixes in the laboratory using the temperature cycling method of Stern *et al.* (2004). We had originally considered making hydrate separately and transferring it to the conductivity cell at liquid nitrogen temperature and room pressure, but during the design phase of this project we realized that it would be easier, safer, and more reliable to design the cell to allow us to make the hydrate *in situ*. The addition of custom high pressure manifolds to the pressure vessel allows both high pressure methane and an electrical feed-though to share the single pressure port on each end-cap. The cell was constructed at Scripps Institution of Oceanography and tested using teflon blanks (to test for electrical leakage) and water ice, and then shipped to Laura Stern's laboratory at the U.S. Geological Survey Menlo Park campus for the hydrate measurements. The cell is loaded with seed ice and then placed under methane pressure in a temperature controlled bath of inert coolant. The first run was carried out with one manifold replaced by a thermocouple, to calibrate the synthesis reaction. Subsequent runs could then be carried out without the thermocouple, using the electrical conductivity as an indicator of when the ice/water transitions occurred. Cryo-SEM images were used to confirm that the synthesis was successful (Figure 2). The resulting hydrate had a porosity of about 20% and gain sizes of 20–70 μm.
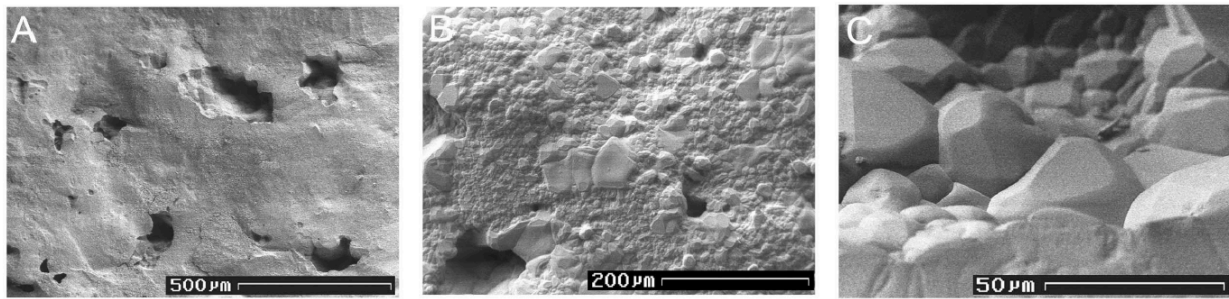
Figure 2. Cryo-SEM images of methane hydrate synthesized in run 1, use to calibrate the synthesis process.

Electrical conductivity measurements were carried out by collecting impedance spectroscopy data using an Agilent E4980A LCR meter, which measures complex impedance at frequencies of 20 Hz to 2 MHz. The resulting Cole-Cole plots (Figure 3) exhibit approximately semi-circular arcs associated with the equivalent capacitance and resistance of the sample components, most typically the electrode surfaces and the sample interior. By modeling the equivalent RC circuits we can separate the effects of the blocking (polarizing) electrodes from hydrate conductivity.
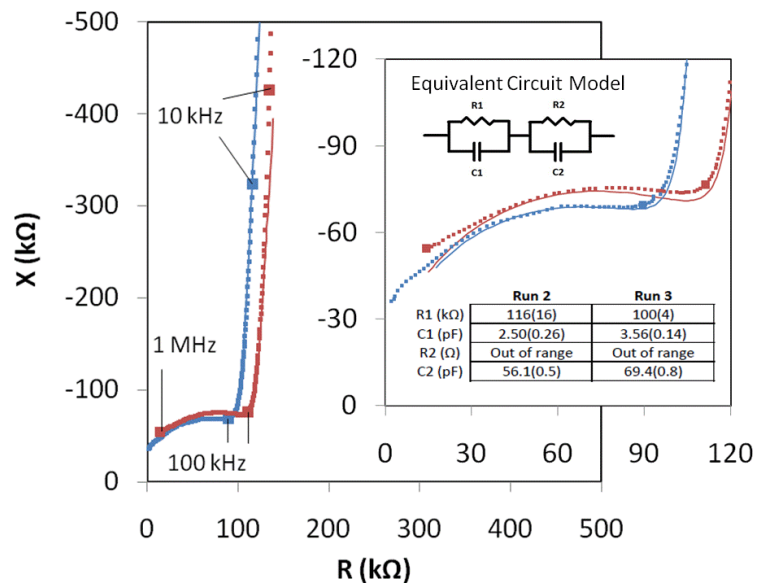

Figure 3. Spectral impedance plot of one hydrate conductivity measurement. Equivalent circuit analysis (inset) allows us to separate the blocking (polarizing) effect of the electrodes from the sample conductivity.

Two runs were made to measure the conductivity σ of pure methane hydrate (Figure 4), using independent syntheses from two charges of seed ice. The agreement between the two runs is excellent. The conductivity is four times lower than the seed ice and shows the characteristic linear behavior in the log(σ) versus reciprocal temperature plots (Arrhenius plots) of a thermally activated Boltzmann process. This may be modeled by an activation energy E_a using

$$\sigma(T) = \sigma_0 e^{-E_a/(RT)}$$

where σ_0 is the pre-exponential constant and R is the gas constant. The resulting activation energies are 27.9 and 30.6 kJ/mol for the two runs. The last run (blue in Figure 4) is considered slightly more reliable because the sample was allowed to equilibrate at each measurement temperature until the conductivity ceased changing before measurements were made. The resistivity at 0°C is 20,000 Ωm, which is a considerably lower conductivity than that of the starting ice mixture. Although it has been known for decades that hydrate is electrically resistive, these are the first quantitative results documenting the magnitude and temperature dependence of the electrical properties. In Section 5 of this report we use this temperature dependence in the estimation of hydrate volume from electrical resistivity measured in the field.
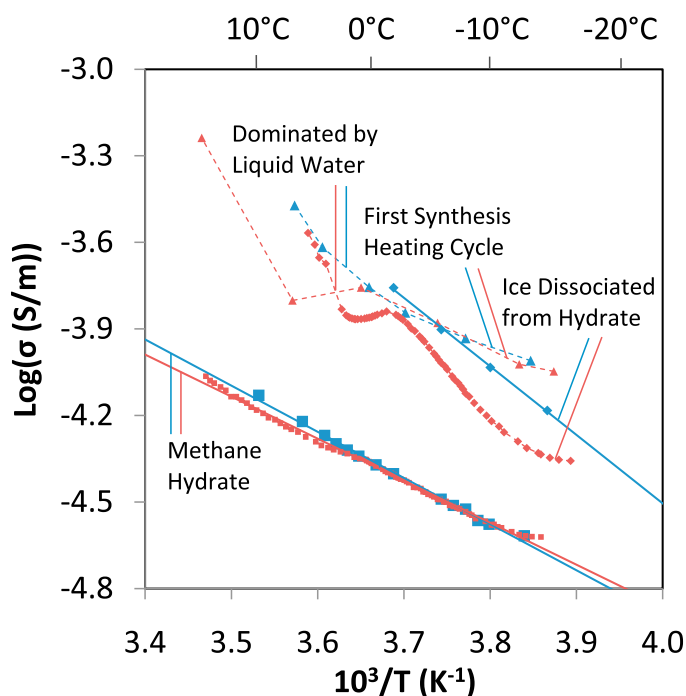

Figure 4. Electrical conductivity versus reciprocal temperature for pure methane hydrate and the ice/water from which it was synthesized (from Du Frane *et al.*, 2011a). There are two independent runs shown here, in blue and red.

Our next runs were made on various mixtures of methane hydrate and sand (OK#1). The interesting feature of these data (Figure 5) is that as the percentage of sand, a nominal insulator, is increased from 0% to 50%, the conductivity of the assemblage *increases*. We interpret this to mean that the hydrate/sand interface increases the conductivity of the hydrate. When 90% sand is added, the percolation threshold is reached and hydrate grains are no longer in continuous contact across the sample, resulting in a large drop in conductivity. This suggests that it is not the sand surfaces that provide the conduction pathway, but rather the hydrate surfaces. However, when we replicated the experiment with pure silica beads (Figure 6), we do not get such an enhanced conductivity, suggesting that it is not simply the surface area of hydrate that is the determining factor in conduction. We have yet to fully understand these results, but they clearly show that simple mixing laws, such as Archie's law, may not provide correct concentrations of hydrate in the case of reservoir sands fully permeated with hydrate. Figure 7 shows some of the cryo-SEM studies used to characterize the samples from the conductivity runs. These images demonstrate that our samples are similar to those found in nature, increasing our confidence that the results are representative.

Figure 5. Electrical conductivity versus reciprocal temperature for mixtures of methane hydrate and silica sand (modified from Du Frane *et al.*, 2011b).
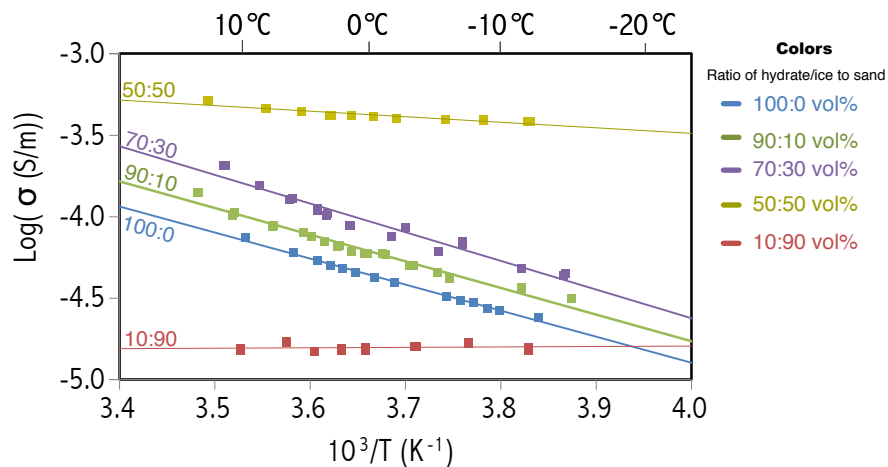
Figure 6. Electrical conductivity versus reciprocal temperature for 50:50 mixtures of methane hydrate and glass beads and methane hydrate and silica sand (modified from Du Frane *et al.*, 2011b).
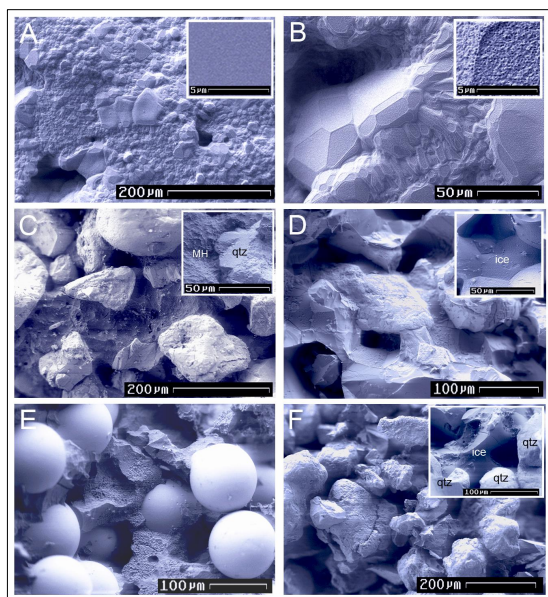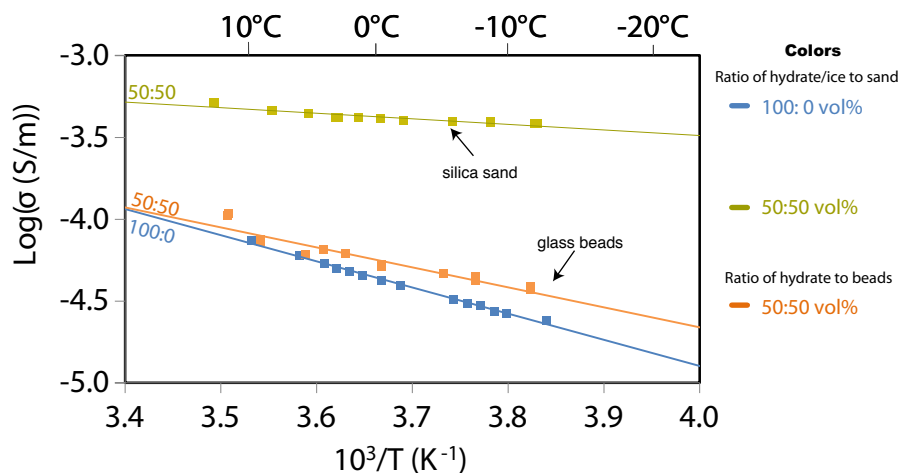

Figure 7. Cryo-SEM images of hydrate-sediment mixtures. A and B show single-phase (unmixed), polycrystalline CH_4 hydrate with 20% porosity. Hydrate grains typically range 10-80 μm in diameter and are fully dense as-grown (A, inset) but develop surface pitting with time in the high-vacuum SEM column (B, inset). C shows a 50:50vol% hydrate:sand sample and D shows a 50:50vol% ice:sand sample. Significant annealing of the ice grains accompanies dissociation at our test conditions (compare D and C insets), but there is no significant migration of sand, thus enabling comparison of measurements before and after dissociation. E shows a 50:50vol% hydrate:glass bead sample. SEM shows uniform distribution of phases in all three samples (C, D, and E) as well as similarities in the nature of the grain contacts, helping establish a basis for comparison of conductivity measurements. F shows a 10:90vol% ice:sand sample, with some of the connecting ice expanded in the inset.

3. TOTAL FIELD NAVIGATION OF TRANSMITTER POSITION

We carried out an 18-day cruise on the R.V. Roger Revelle in the Gulf of Mexico from 7th–26th October 2008 to collect controlled-source electromagnetic (CSEM) data over several hydrate prospects. During this experiment we deployed 30 ocean bottom electromagnetic (OBEM) recorders a total of 94 times at four survey areas and towed the Scripps Undersea Electromagnetic Source Instrument (SUESI) a total of 103 hours. SUESI transmission was 200 A on a 50 m dipole antenna at heights of 70–100 m above the seafloor. We also towed a 3-axis electric field recorder behind the SUESI antenna at a constant offset of 300 m.

We carried out two types of CSEM surveys – a traditional setup in which sea-floor EM receivers collect data broadcast by a transmitter towed close to the sea-floor behind the research vessel, and a new approach developed specifically for hydrate mapping, in which an EM receiver is towed a constant offset behind the transmitter. Although the constant-offset towed receiver data can be processed without accurate transmitter positioning, fairly precise acoustic location of the transmitter position is required for the processing of sea-floor receiver CSEM data.
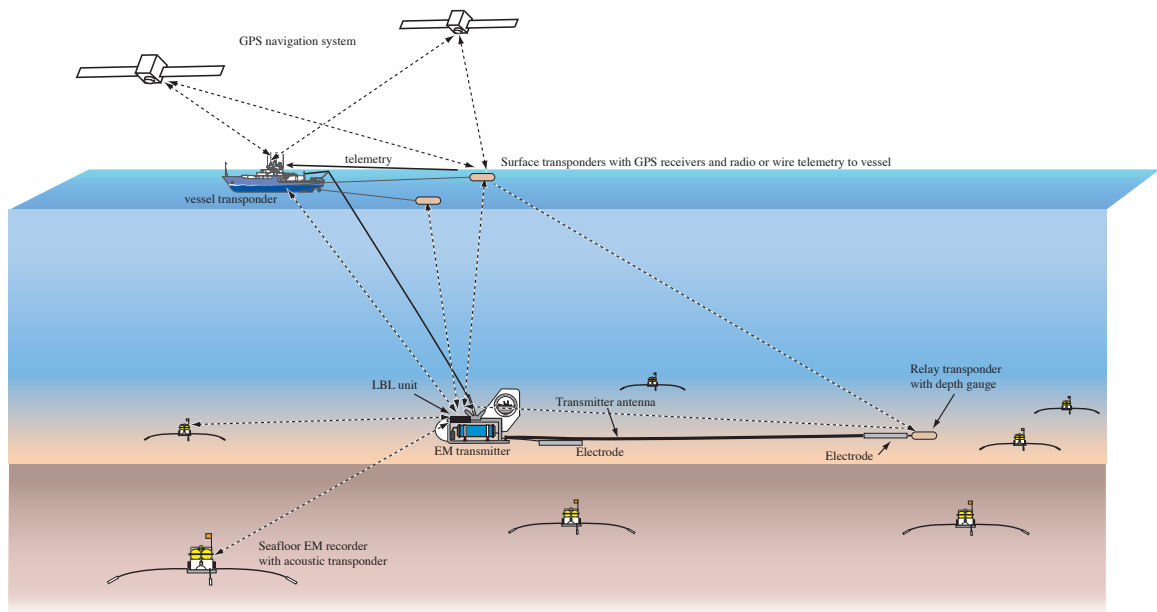

Figure 8. Inverted long-baseline acoustic navigation system for CSEM transmitter location. Two acoustic transponders are towed on paravanes behind the research vessel, equipped with GPS receivers which use radio telemetry to send position data to the ship. An acoustic ranging system on the deep-towed transmitter ranges to the surface transponders, sending the ranges to the ship via the tow cable, along with depth information from an on-board pressure gauge. These data may then be used to triangulate the position of the transmitter in real time. A relay transponder on the antenna can also be used to obtain information on antenna set.

Deep-towed EM transmitters are conventionally navigated using a short-base-line (SBL) or ultra short base-line (USBL) acoustic systems, but these have several deficiencies. Firstly, until recently USBL systems did not work in water deeper than a couple of kilometers, while one of our Gulf of Mexico surveys was carried out in water deeper than 3,000 m. Secondly, while the specifications for precision are quite good, in practice we have seen errors of up to 50 m in transmitter locations surveyed with USBL systems. Performance is particularly poor for rented systems installed temporarily on research vessels, which is the way research groups such as ourselves have to operate (the systems are also quite expensive). Finally, USBL systems have a limited angle of operation, and if the layback of the transmitter increases too much it can be completely lost from vision. This problem is particularly relevant for the location of the far end of the antenna, and makes the system largely useless for location towed receivers some hundreds of meters behind the transmitters.

In deepwater operations the traditional alternative to SBL systems is to use long baseline (LBL) acoustic navigation

using an array of moored transponders. It takes considerable time to install and recover LBL arrays, and either the survey area has to be kept small or the transponder arrays have to become large. For our Gulf of Mexico surveys, we planned to implement a newly developed inverted long-baseline acoustic navigation system in which the transmitter package ranges on surface transponders to triangulate position (Figure 8). While we had successfully tested this system off San Diego, this was the first operational application of the new equipment, and unfortunately we had technical problems which prevented us collecting useful navigation data until the end of the research cruise. Our problems making this new system work were exacerbated by the program we had chosen, in which we collected data from the prospect in deepest water first. We addressed the lack of acoustic navigation data by developing the scheme described in this section, in which the transmitter location is derived from the geometry of the CSEM fields, and which we call Total Field Navigation (TFN).

The idea behind TFN is that near-field electric and magnetic data (less than 1 km in source-receiver offset) collected by sea floor receivers are poorly sensitive to sea floor resistivity, and can be used to recover the geometry of the transmitter. This is essentially a parameterized inverse problem, and we use both the Levenberg-Marquardt and Occam inversion schemes to solve for navigational parameters including transmitter position (x, y), antenna azimuth (θ), antenna dip (ϕ), and half-space resistivity below the transmitter (ρ). Receiver positions and orientations are well constrained by LBL navigation from the ship and recording pitch/roll/heading sensors. The inversion algorithm uses the one dimensional dipole forward modeling code, Dipole1D of Key (2009), and requires an initial model of half-space sea floor resistivity and an initial geometry of the transmitter and receivers. The algorithm updates the model parameters until convergence is reached between the synthetic EM responses and the observed EM data.
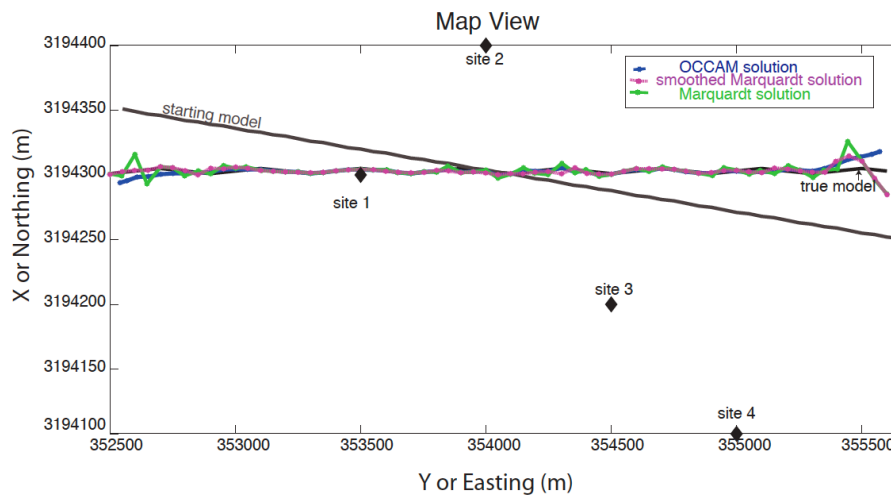

Figure 9. Receiver site distribution, starting model, true model, and TFN solutions for the (x, y) positions of the synthetic model study.

A synthetic model was used to test and verify the accuracy of the Marquardt and Occam total field navigation codes. We generated synthetic electric (Ex; Ey; Ez) and magnetic (Bx; By) field responses for a 1 Ωm half-space with 63 transmitter positions (x, y, z, azimuth, dip) and 4 receiver positions (x, y, z) using the Dipole1D forward code. We contaminated these responses using a combination of 10% random gaussian noise and a noise floor of 10^{-15} V/Am^2 for electric field data and 10^{-17} T/Am for magnetic field data. The data as used are electric and magnetic fields at ranges <1000 m, giving a total of 2178 data points. Real and imaginary components of the data are used to remove the difficulty in unwrapping phases, which can otherwise easily result in residuals offset by factors of 360°. The total field navigation inversion codes were then used to find the 'true' transmitter positions . Figure 9 shows the starting model and the true solution for the x and y positions of the transmitter.

Figure 10 shows the final models and the differences between the final solution and the true solution for easting, northing and azimuth. In the Occam inversion scheme, the starting model had an RMS of 23 and ran to an RMS of

2.0 in 12 iterations, then converging to an RMS of 1.0 in 6 more iterations. The final model with RMS 1.0 is shown in Figure 10 in blue. There are some subtle differences between the Marquardt and Occam schemes in the center part of the tow and much larger differences are at the ends of the tow lines. The largest variations are at the ends of the tow and for the northing component (up to a 50 m difference). This region is the least well constrained because the transmitter position is only observed by a single receiver. We have also tested solving for a half-space resistivity (ρ) at each transmitter, in addition to the x,y, and azimuth parameters. Increasing the number of free parameters creates more disagreement at the ends of the lines between the final solution and the true solution. These model tests demonstrate the accuracy of the method and provide some guidance when solving for the transmitter position from real CSEM field data.
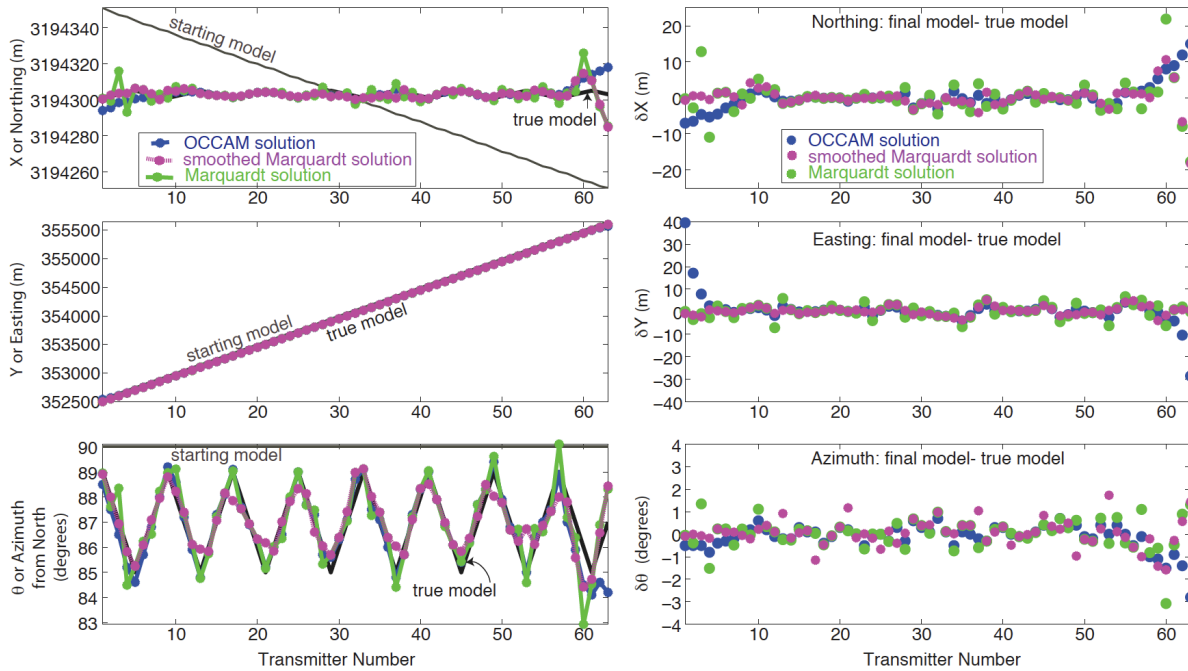

Figure 10. TFN solutions for the (x, y) positions and antenna azimuth for the synthetic model study (left) and residuals after subtracting the true model (right).

Although we did not get the inverted LBL system working in time for our Gulf of Mexico surveys, the experience we gained allowed us to make it fully functional for a CSEM survey carried out the following year in 2009, offshore northwestern Australia. We can use these well-navigated data as a test for the total field navigation code.

A small segment of data was selected, consisting of a single line with 6 receivers spaced approximately 500 m apart, allowing multiple receivers to observe the transmitter at the same time (Figure 11). The 300 A transmission-waveform was a binary double symmetric waveform with a fundamental frequency of 0.25 Hz and the highest power at 0.75 Hz (see Myer et al., 2010). For this CSEM tow a 1D approximation is made for the profile by assuming an average water depth of 937 m. The transmitter's altitude data are used to set the depth of the transmitter by subtracting it from the water depth. The dip of the transmitter antenna is about -5° and was computed by data collected from two depth gauges: one on the tail of the antenna, the second on the transmitter. A seawater conductivity-depth profile was collected by the transmitter's CTD (conductivity-temperature-depth) gauge and is used in the layered 1D resistivity model, along with a final terminating sea floor resistivity of 1 Ωm. The finite dipole length of 250 m was used in the forward calculations.

The total field navigation program accepts unrotated data (i.e. in their individual channels) to eliminate cross contamination of noise from one channel to the other when the data are rotated into an absolute reference frame, so we use the
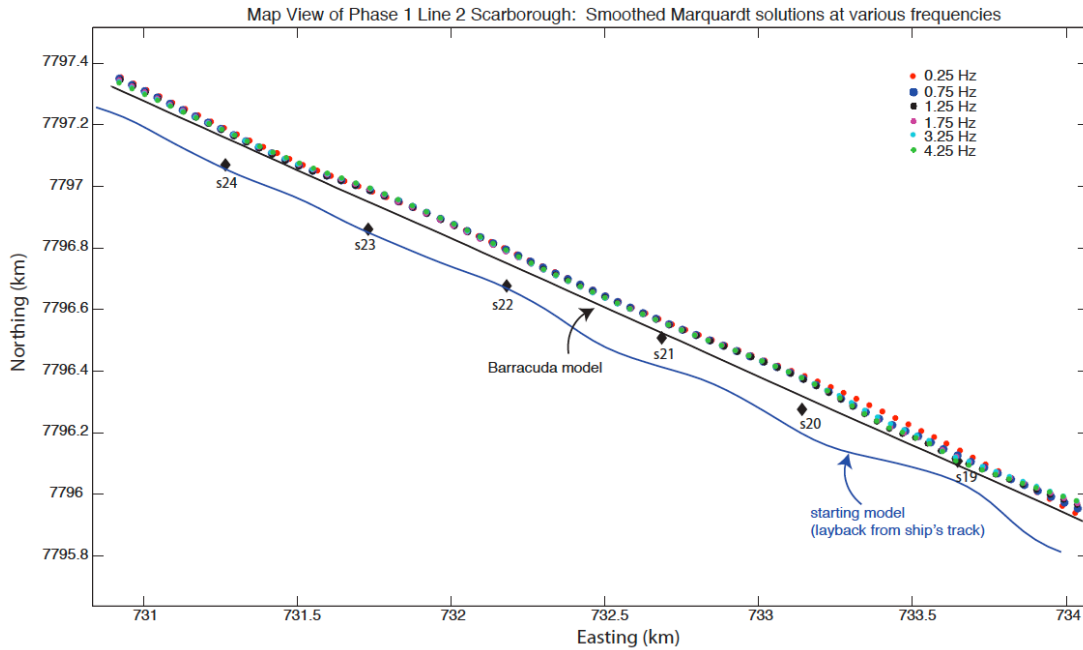
Figure 11. Map view of the receiver positions, starting models, and final models used in the real Australian data example. Barracuda is the colloquial name for our inverted LBL system.

receiver compass orientations and tilts to rotate the model into receiver coordinates. We use the horizontal electric and magnetic fields at ranges less than 1 km, which are well above the instrument noise floor. The data are assigned a 10% error in amplitude which is applied equally to the real and imaginary components to account for random and geologic noise. During the survey the transmitter was towed at 50 m height above the sea floor, and electric and magnetic receiver channels saturated at ranges less than about 450 m. From experience we know that saturated magnetic field data are not usable but saturated electric field phases are. Since we use of real and imaginary components for the inversion to avoid dealing with phase wrapping we need to reconstruct the saturated data so we can still use the phase data. To do this, when amplitudes are saturated a fake amplitude of 1 was used to compute the real and imaginary components from phase data.

For the Marquardt solution of this particular data set we solved for transmitter x, y, and azimuth using 4.25 Hz receiver data, and found that the selection of a fixed 1 Ωm or a 2 Ωm half-space resistivity had no effect on the final Marquardt model. We also tested different starting models: 1) Assuming the transmitter follows in the ships track and backing out transmitter position based on wire out, altitude and depths; and (2) from the inverted LBL navigation solution. We found that there were differences between the two final transmitter solutions, mainly at the closest approach of the transmitter to the receivers that are at the end of the line. This problem is caused from a lack of data, since with fewer receivers observing the same transmitter position the inversion has less constraint placed on the final solution. The inversion can find a zero crossing by either narrowing in on the cusp at the closest approach (inverted LBL solution) or by moving farther away from the receiver (Ship's track solution). Note that using Occam inversion prevents some of this erratic behavior by smoothing neighboring points.

We tested the inversion using different frequencies (0.25 Hz, 0.75 Hz, 1.25 Hz, 1.75 Hz, 3.25 Hz, and 4.25 Hz) and found a slight frequency dependence on the final model (Figure 12). In general all of the Marquardt solutions follow a similar trend, with the exception of the fundamental frequency of 0.25 Hz. The behavior of the 0.25 Hz model suggests that the method is exploiting inductive propagation losses in seawater as well as low frequency field geometry. We expect the 0.75 Hz data to be the best data to use for navigating the transmitter, as it has the highest power and is low enough that any superficial or local resistivity structure will have little effect on the data.
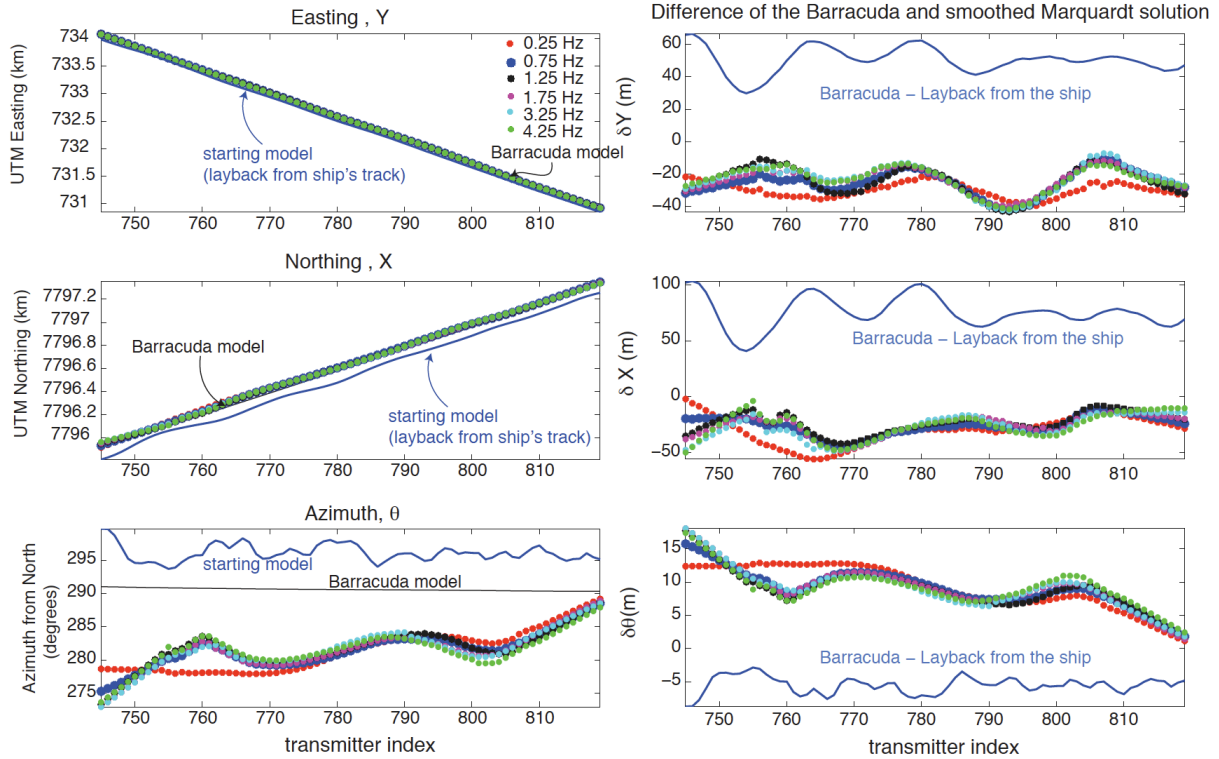
Figure 12. TFN solutions for the (x, y) positions and antenna azimuth for the real data study (left) and residuals after subtracting the inverted LBL (Barracuda) model (right). The blue lines show the difference between positions estimated from ship path and those determined using the inverted LBL system. Note that the inverted LBL system did not estimate antenna azimuth, and the 291° estimate for azimuth is an approximation.

The starting model using the layback from the ship for the transmitter position places the transmitter incorrectly to the south of all the receivers and several hundred meters from the navigated solutions. However, the final model is within a few tens of meters from the LBL navigated solution. The estimated error on the LBL navigated solution is 5–10 m, and so it is hard to determine if the difference between the navigated LBL positions and the TFN positions is a result in an error in the TFN or the original navigation. For the antenna azimuth the LBL estimate is not based on acoustic data, but rather a projection of the crossline offset into the antenna direction. Given the good performance of the TFN algorithm in recovering azimuth in the synthetic test, there is reason to believe that the TFN solution is the more accurate one.

Finally, in Figure 13 we show the effect of applying the TFN algorithm to data from the Gulf of Mexico hydrate survey. These images are apparent resistivity pseudo-sections, in which a half-space resistivity is estimated for each data point and which is then plotted below the source–receiver midpoint at a depth proportional to source–receiver offset. This will be discussed in more detail later in this report. The left plot is an initial navigation model based on ship's position and transmitter layback, and the right plot shows the TFN solution. It can be seen that the TFN algorithm has removed artifacts near sites 9 and 12, and made the target structure under site 7 much more coherent.

4. GULF OF MEXICO CSEM SURVEYS

Over the last decade, marine CSEM methods have been adopted by the oil and gas industry as a deepwater exploration tool. Ocean-bottom electromagnetic (OBEM) recorders are deployed on the sea floor and a powerful EM transmitter is towed through this array in close proximity (50–100 m) to the sea bed (Figures 8 and 14). In this way data are collected to transmitter–receiver offsets of many kilometers and sensitive to depths of several kilometers into the crust. One of the principle applications of this relatively new technology is discriminating between seismic targets that are
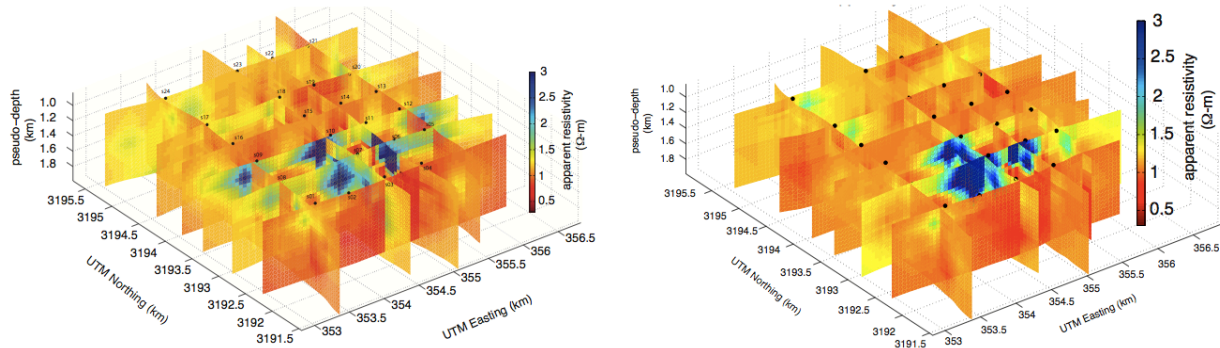
Figure 13. Apparent resistivity pseudo-section computed with navigation from layback and ship's track (left) and the total field navigation algorithm (right), for 6.5 Hz data collected over MC 118 in the Gulf of Mexico. It can be seen that artifacts near sites 9 and 12 have been removed, and the target structure under site 7 is made much more coherent.

caused by a small amount of gas in the pore volume ("fizz-gas") and viable hydrocarbon reservoirs, which are more resistive. We had successfully used this traditional CSEM method to study hydrate offshore Oregon at Hydrate Ridge, and applied it as one component of the Gulf of Mexico surveys in this project. However, a sparse array of sea floor receivers is not ideal for studying structure in the upper few hundred meters of sediment. To address this problem we developed a three-axis electric field receiver that may be towed at a fixed offset of 300–1,000 m from the transmitter ("Vulcan"). Unlike similar systems that are dragged in contact with the sea floor, by "flying" the receivers at a similar height to the transmitter we can operate in areas with installed infrastructure such as well-heads, pipelines, and so on. This complicates the problem of locating the positions of the instruments, but the towed receivers record depth, pitch, roll, and heading as well as electric field amplitude and phase.
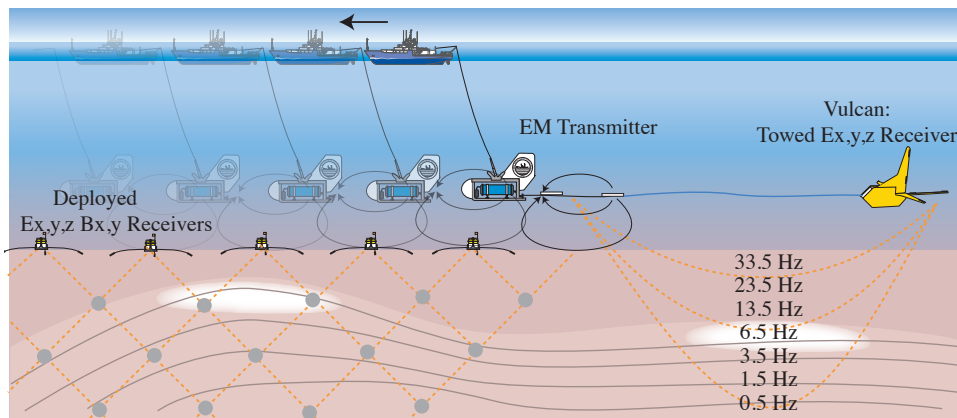

Figure 14: Marine CSEM system showing deployed OBEM instruments and the towed 3-axis electric field receiver called Vulcan. We can build apparent resistivity pseudosections two different ways: The left side shows apparent resistivities derived from OBEM instruments projected to a mid-point between the EM transmitter and receiver, at a pseudo-depth proportional to the transmitter-receiver offset. For the fixed-offset towed receiver (right), apparent resistivities from different frequencies can be projected at the common mid-point based on skin depth, with lower frequencies having larger skin depths/deeper penetration.

For traditional CSEM surveys with deployed OBEM receivers, the various transmitter–receiver offsets provide depth sensitivity in the data, since larger offsets are associated with more deeply penetrating fields. For the fixed-offset towed receiver we can use transmitter waveforms with broad frequency content to provide sensitivity at different depths, since high frequency EM energy gets absorbed more rapidly in conductive sea floor sediments, while low frequency energy can propagate more deeply. We can thus use the characteristic penetration distance, or skin depth, as a depth discriminator.

We will present data from the Gulf of Mexico surveys in pseudosection form. To obtain pseudosections we generate an apparent resistivity for each data point by comparing the magnitude of the major axis of the data polarization ellipse with half-space forward models. A pseudosection projection technique is then used to plot the data. Figure 14 (left) shows a schematic of the data projection for mapping ranges from OBEM receivers into depths; the longer the transmitter-receiver offset the deeper that data point is projected. A similar approach is taken with the Vulcan data except that the Vulcan apparent resistivity pseudosections are generated as a function of frequency, using skin depths for each frequency as a length scale, as shown in Figure 14 (right). Pseudosections provide a way to observe lateral variations in resistivity and give qualitative depth relationships. However, they do not provide quantitative depth information, and so the depth scales in the following figures should not be taken literally.

We had been working closely with industry for several years prior to the start of this project to design a field program to collect marine EM data over a hydrate prospect in the Gulf of Mexico. Our initial goal was to pick a single, well-characterized hydrate site and carry out a very dense, comprehensive survey there. However, during discussions and planning it became clear that such a single ideal site did not exist. At a meeting in Austin, Texas, on the 5th January 2007, a group of 20 industry and academic representatives discussed candidate sites for a project under the revised philosophy that no ideal target existed in the GoM and that as many locations as possible should be surveyed. Three sites (Figure 15) were chosen. A fourth site (WR 313) was later added at the request of DoE. We collected data during an 18-day cruise on the R.V. Roger Revelle in the Gulf of Mexico from 7th–26th October. During this time we deployed 30 ocean bottom electromagnetic (OBEM) recorders a total of 94 times at the four survey areas and towed the Scripps Undersea Electromagnetic Source Instrument (SUESI) a total of 103 hours. SUESI transmission was 200 A on a 50 m dipole antenna at heights of 70–100 m above the seafloor. We also towed a 3-axis electric field recorder behind the SUESI antenna at a constant offset of 300 m. Only two seafloor deployments failed to collect data, and data quality was excellent on all the rest.
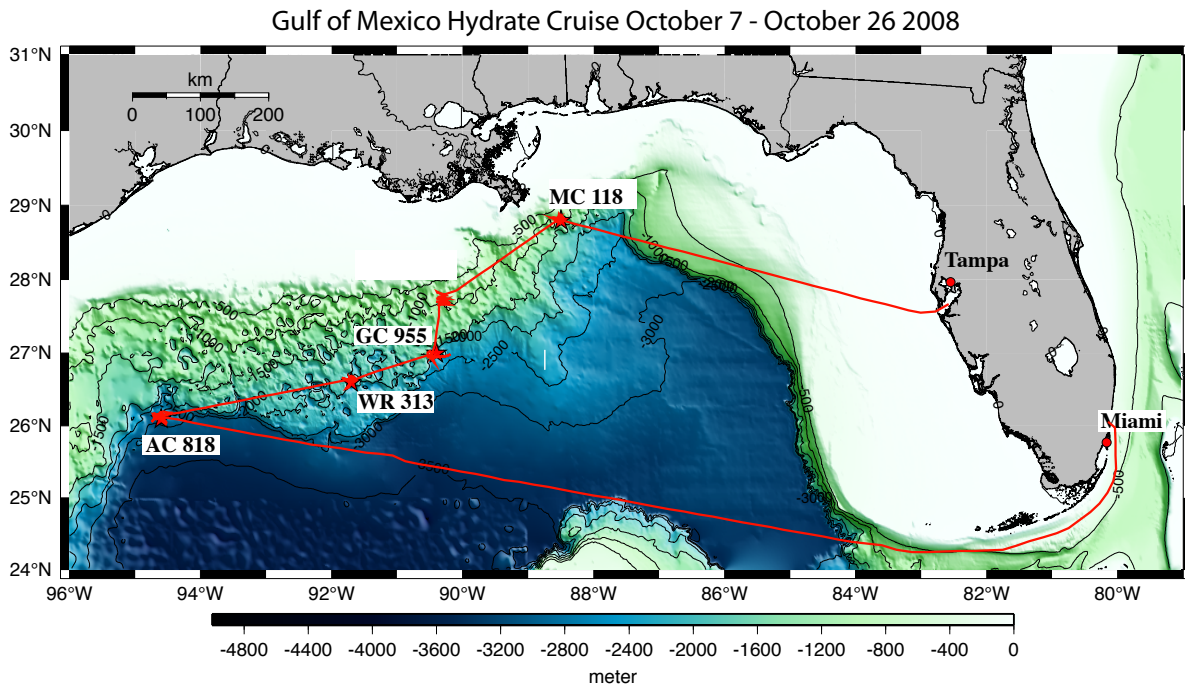
Figure 15. Map showing the survey locations in Alaminos Canyon (AC 818), Mississippi Canyon (MC 118), Green Canyon (GC955), and Walker Ridge 313 (WR 313), along with the Miami to Tampa route taken for the project.

As an introduction to the data sets, we present brief descriptions of the four sites, why they were chosen, and the data recovery:

Alaminos Canyon 818. Chevron encountered a thick hydrate-bearing section (20 m) a few hundred meters below seafloor in an exploration well on this block, with high resistivities (30–40 Ωm) evident in the logs. Water depth is around 3,000 m, which is deep for exploration but easily within the 6,000 m operating depth of our equipment. Initially we were hoping to impact future Joint Industry Project (JIP) drilling plans, but shortly before the cruise we heard that AC 818 was dropped from the JIP program. However, at that time it was one of the few places in the Gulf where hydrate has been found in the sub-section (c.f. the seafloor), and this area remained the highest priority for our own studies. We deployed 30 receivers and made four transmission tows, centered on the Chevron well. Two instruments failed to record data.

Green Canyon 955. This prospect is in intermediate water depth (2200 m) and shows evidence of gas accumulation in a channel sand near the base of the hydrate stability field, based on examination of seismic data. It is targeted by the JIP program, but unfortunately current exploration drilling prevented us from carrying out our planned survey. We deployed 20 seafloor instruments (all of which collected data) along two transmission lines as close as possible to the anchor patten of the drill rig that was occupying the block at the time of our survey.

Walker Ridge 313. This prospect was added at the request of NETL. It is in intermediate water depths on the lower slope of the northern Gulf of Mexico, within a tabular salt minibasin province and having a very low geothermal gradient (hence a very thick gas hydrate stability zone). Evidence for hydrate comes from seismic data, gas mounds, and focused fluid expulsion sites. WR 313 is the third location chosen for the JIP (along with GC 955 and AC 818), and so clearly it is desirable to have marine EM data for comparison with the drilling results. We decided that if we had cooperative weather and scaled back the GC 955 survey by a few sites it would be possible to carry out a two-line survey similar to the one at Green Canyon. We deployed 20 receivers in two intersecting lines and towed the transmitter and Vulcan over top of the receivers. Again, we had 100% data recovery.

Mississippi Canyon 118. This block has been designated as a Minerals Management Services (now BOEM) observatory. Large outcrops of hydrate occur on the seafloor in relatively shallow water depths of 800–900 m, but there is yet no direct evidence of hydrate at depth. This area provides the opportunity to coordinate and collaborate with many other ongoing scientific programs, including shallow resistivity surveying. We deployed 24 receivers in a 6 x 4 array and towed 10 transmitter lines in a grid pattern (avoiding the already installed seafloor equipment). All receivers recorded data.

Alaminos Canyon 818. The AC 818 OBEM 0.5 Hz pseudosections are shown in Figure 16 (centre) with a closer examination of the EW-trending CSEM Line 1 (bottom) and NS-trending Line 2 (top). An EW seismic line and an estimate for gas hydrate distribution in the Frio sand derived from a 3D seismic volume as presented in Boswell et al. (2009b) are also included in the figure.

All four pseudosections display a consistent image; for example all three NS trending pseudosections have a conductive region to the north-east (NE of sites 30, 18 and 19). The AC 818 pseudosections have a more complex resistivity structure when compared with the MC 118 pseudosections shown in Figure 13 above (also true of the WR 313 and GC 955 pseudosections discussed below) and the background resistivity at AC 818 is higher than MC 118, varying from 1.5 to 2 Ω-m. A resistive region trends from the NE to the SW, and is consistent with the map view of the seismically derived hydrate distribution given in Boswell et al. (2009b). The NE to SW OBEM Line 2 pseudosection (Figure 16 top) has a large resistor to the north (site 16) and to the south (site 13 and 14), a pattern of conductive and resistive sediments that could be associated with the pattern of water saturated sand and hydrate-bearing Frio sand (Figure 16 left) given in Boswell et al. (2009b). The NW to SE OBEM Line 1 pseudosection (Figure 16 bottom) has a resistive region (sites 9 and 8) associated with the shallow salt indicated in the seismic section. Seismic bright spots have been documented by Latham et al. (2008) and Hutchinson et al. (2008) and are thought to be associated with free gas. The pseudosections have a resistive region which may correspond to this seismic event (site 7). At the well location itself there is a very subtle resistive region in the shallow section, which could be associated with the LWD resistive region discussed in Smith et al. (2006), but more likely the NE to SW tows are capturing this resistive region. Under sites 5

Seismic Image from Boswell et al., (2009) *Marine and Petroleum Geology* Fig. 2
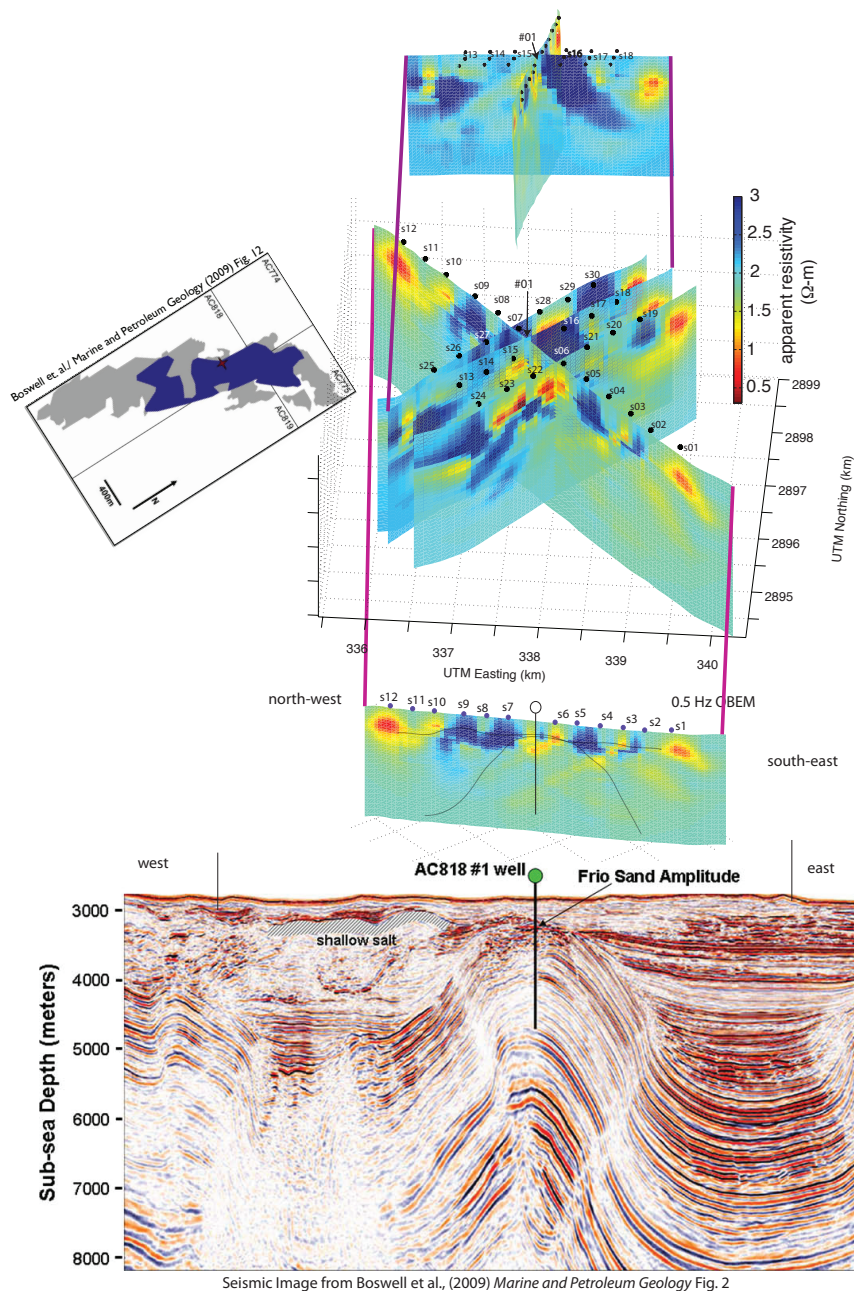
Figure 16: OBEM pseudosection crossplots for AC 818 at a frequency of 0.5 Hz and a closer examination of Line 1 (bottom) and Line 2 (top) with corresponding seismic data. The bottom seismic line is an EW transect showing where the Oligocene Frio sand is above the gas hydrate stability field (labelled as Frio Sand Amplitude) (Boswell et al., 2009b). The left map view shows in blue the gas hydrate distribution within the Frio sand and in grey the water saturated frio sand with low saturations of free gas (Boswell et al., 2009b).

and 4, a resistive region is present and may be associated with an inferred BSR discussed in Jones et al. (2008). AC 818 is on the Perdido fold 3 (Fiduk et al. 1999) which has pushed the Oligocene Frio sand into the hydrate stability zone (Boswell et al., 2009b, Hutchinson et al., 2008, Jones et al., 2008, Latham et al., 2008). This fold is shown in the EW seismic section and our pseudosections show it to have a background resistivity of 2 Ω-m, attributed to the water saturated Frio sand.

Green Canyon 955. GC 955 is a prospect in intermediate water depth (1900-2200 m) located seaward of the Sigsbee

Escarpment and at the mouth of Green Canyon, which brings sediments onto the deep seafloor. There is surface evidence of features often associated with hydrate, such as mud volcanoes. A surface channel is present in the bathymetry and channel sands are present at depth. One such channel sand was a target of the JIP, and is well defined in seismic data, which shows evidence of gas accumulation near the base of the hydrate stability field (McConnell et al., 2010; Hutchinson et al., 2008; Jones et al., 2008).
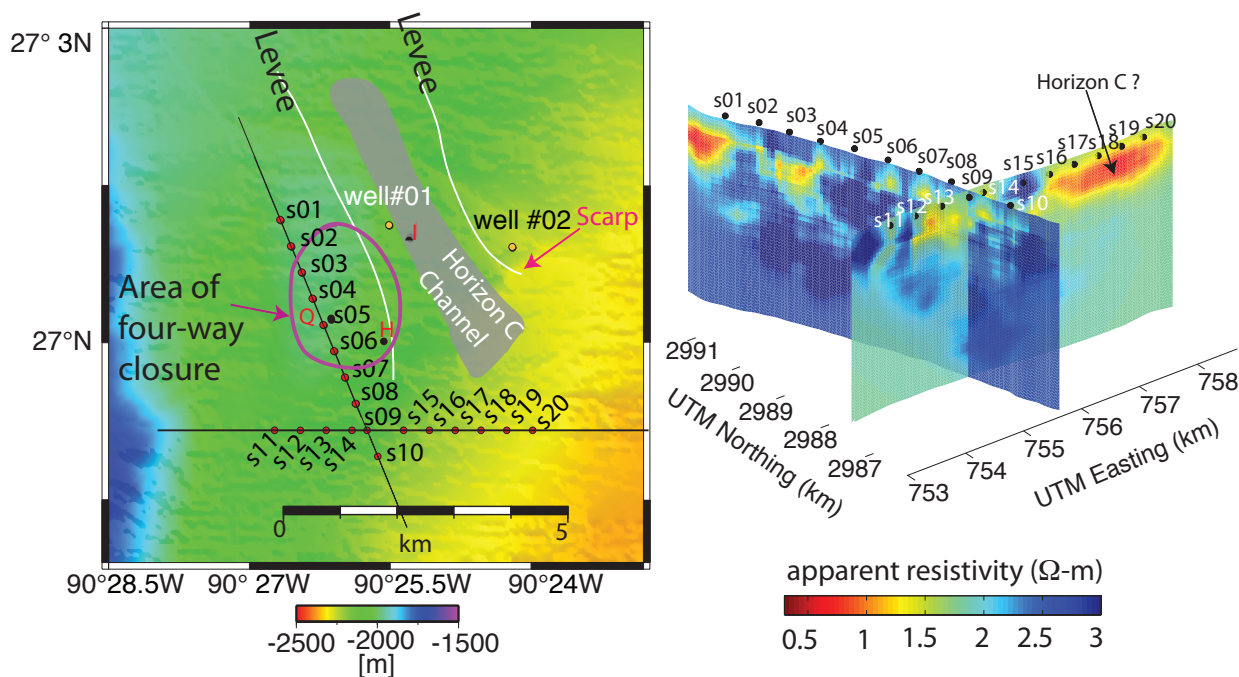
Figure 17: GC 955 survey map with annotations from Hutchinson et al. (2008) (left) and 0.5 Hz OBEM pseudosections (right).

We deployed 20 seafloor instruments along two transmission lines as close as possible to the anchor pattern of a drill rig that was operating on this block during our survey (Figure 17). For this reason the CSEM lines do not directly intersect the JIP drill locations. The N-S CSEM line is located in an area of four-way closure consisting of a bathymetric high cored by allochthonous salt above which sandy levee sands are sealed by a regional shale layer (Hutchinson et al., 2008). Faults here provide migration pathways for fluids (Hutchinson et al., 2008). This allochthonous salt is a large regional feature that is hour-glass shaped and extends to the south into Walker Ridge (McConnell et al., 2010 and references therein). Seismic horizon C, shaded in grey, is a channel sand expected to contain gas hydrate (Hutchinson et al., 2008), and which may extend to our E-W CSEM line. A horseshoe shaped scarp face also exists to the east, which likely resulted from internal failure due to fluid flow and gravitational forces at over-pressured sand cropping at the base of the Sigsbee escarpment (McConnell et al., 2010 and references therein). A similar process is likely occurring below the E-W line to the east of the area of four-way closure, where there is an amphitheater-shaped region of seep sapping (McConnell et al., 2010).

Pseudosections for the E-W and N-S CSEM tows are shown for the OBEM receivers at the fundamental frequency of 0.5 Hz in Figure 17 (right). One main observation is that the N-S CSEM line is more resistive than the E-W CSEM line. This is likely caused by a regionally extensive N-S trending allochthonous salt body present along this line. The E-W line is perpendicular to this structure and its pseudosection is not dominated by the presence of salt. Gas hydrates were found in GC 955 well 'H' and 'Q', both targeting hydrate filled sands that are located in the area of four-way closure (McConnell et al., 2010). In addition, well 'H' also encountered fracture-filled hydrate above the sand target. The drilling at well 'Q' had to be aborted due to gas flow, either caused by hydrate dissociation or free gas (McConnell

et al., 2010). The N-S pseudosection is resistive at site s05, consistent with the existence of hydrate in the coincident JIP well 'Q'. The N-S and E-W CSEM lines cross at site, s09 and tie together well.

Figure 18 (left) shows Vulcan and 6.5 Hz and 0.5 Hz OBEM pseudosections for the E-W CSEM line. The three images tell a consistent story: a conductive region to the east (s16 to s20) and more resistive area on the slope of the bathymetry high (s15, s09, s14), grading into an interspersed conductive and resistive region at the actual bathymetric high (s11-s13). The deep resistor in the 0.5 Hz OBEM pseudosection is likely due to the allochthonous salt and the fact that it is barely seen in the 6.5 Hz OBEM pseudosection indicates it is a deep structure. The resistive region below s11 in the OBEM data is observed in the Vulcan data as well, but is offset due to the different projection geometries of Vulcan and OBEM resistivities. JIP well 'H', located on the flank of the area of four-way closure, is about 1 km north of the E-W CSEM line and is roughly between s09 and s15. Drilling at 'H' found a shale section with fracture-filled hydrate which reaches the seabed and then a deeper occurrence of alternating gas hydrate and water pore fill bearing intervals within a single sand reservoir (McConnell et al., 2010). This is consistent with the resistive region between s15 and s14.

Hydrate was expected to be found in well 'I', which was drilled into the axis of the porous sand channel (horizon C), but water saturated sand with very little hydrate or free gas was encountered (McConnell et al., 2010). This channel sand likely extends to the south and is probably expressed as the more conductive region on the east side between s16 and s20.
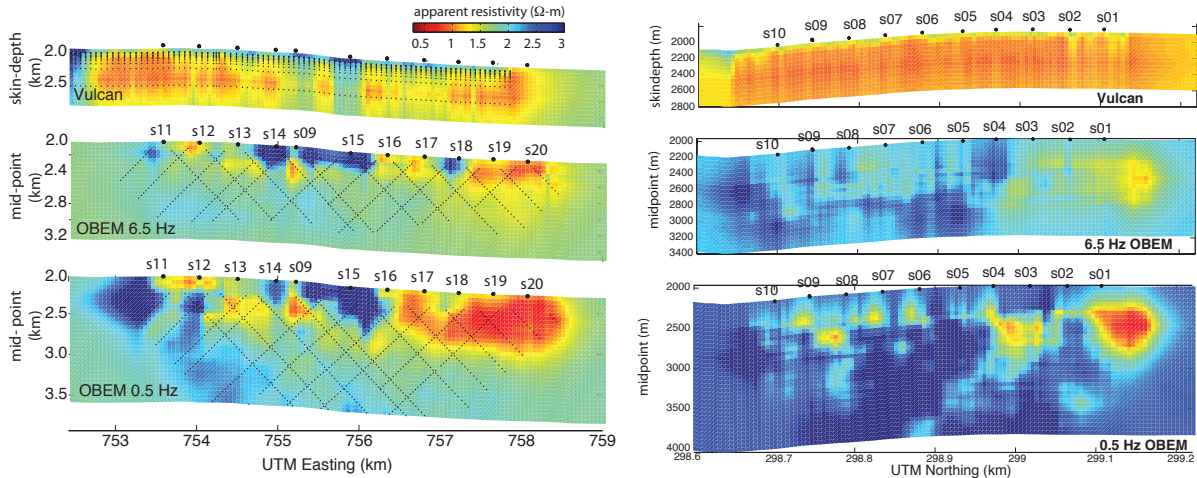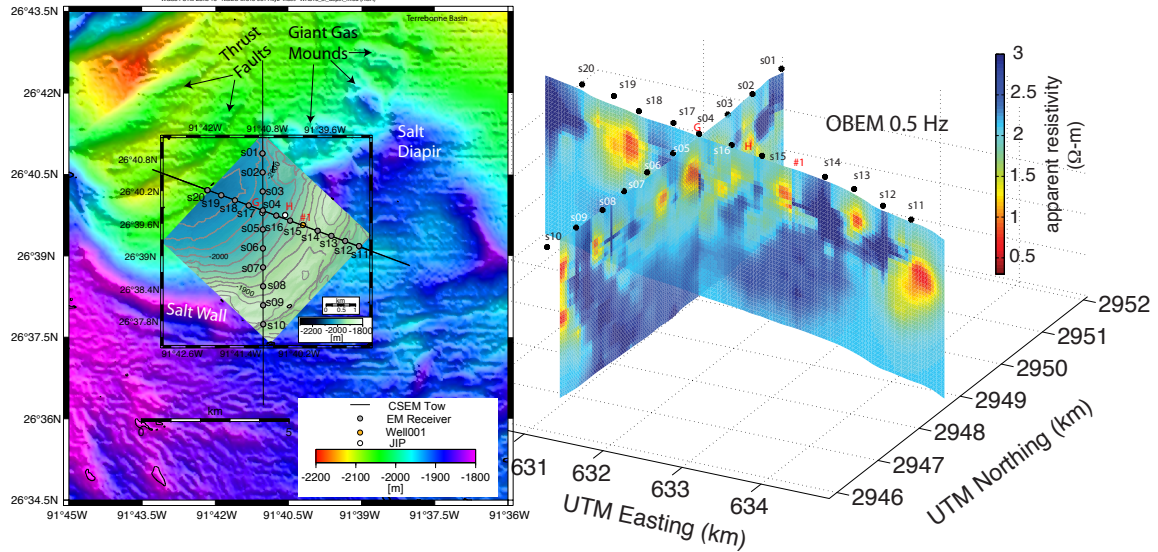

Figure 18: GC 955 EW CSEM line (left) and NS CSEM line (right) for the Vulcan data (top), 6.5 Hz OBEM data (middle) and 0.5 Hz OBEM data (bottom).

The NS tow is shown in Figure 18 (right). The 0.5 and 6.5 Hz OBEM data are dominated by the NS allochthonous salt, but the Vulcan data appears to be insensitive to its presence, being much more conductive than the OBEM data and having very little structure in the electrical resistivity variations across the line. Site 5 is roughly at the location of well 'Q' which had little evidence of gas hydrate in the upper mud-rich sediments despite its proximity to well 'H', which had fracture filled hydrate that reached the seabed (McConnell et al., 2010). In fact evidence for hydrate at 'Q' did not occur until about 430 mbsf in a tight section of the well log, where at a greater depth continued drilling caused gas flow (McConnell et al., 2010). This points out the sensitivity of Vulcan as a shallow surface resistivity mapper. The hydrate along the N-S tow is not expected until deeper in the section and is not detected by Vulcan here. However, there is evidence from well 'H' of shallow hydrate as well as nearby surface expressions of hydrate due to the proximity of a mud volcano, which may be the cause of the shallow resistors are detected along the E-W tow.

Walker Ridge 313. WR313 is in intermediate water depths on the lower slope of the northern Gulf of Mexico, within a tabular salt minibasin province which has a very low geothermal gradient (hence a very thick gas hydrate stability zone). Evidence for hydrate comes from seismic data, gas mounds, and focused fluid expulsion sites. The western

region of the WR 313 basin is blocked by allochthonous salt to the south, east, and west, creating a closed basin allowing for the deposition of sand. Sediment enters from the north and builds up against the salt wall, creating dipping strata of fine grained clays, interbedded silts and fine grained sands in sheets and channel levee deposits (McConnell et al., 2010). Seismic data exhibits phase reversals in steeply dipping strata, which are interpreted as a transition from gas-charged sand to overlying gas-hydrate saturated sand (Hutchinson et al., 2008). Twenty OBEM receivers were deployed in two intersecting lines coincident with a 3D seismic volume, an industry well WR 313-001 and two subsequent JIP well locations 'G' and 'H' drilled in the spring of 2009 at site 4 ('G') and between sites 16 and 15 ('H').


Figure 19: Walker Ridge 313 survey map with annotation from Hutchinson et al. (2008) (left) and OBEM pseudo-section crossplots for 6.5 (top right) and 0.5 Hz (bottom right).
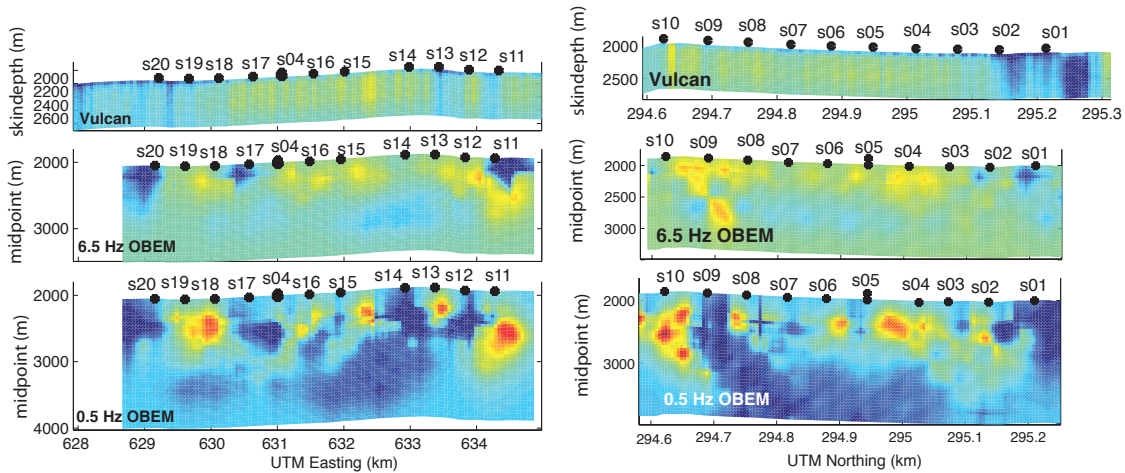
Figure 20: WR 313 EW CSEM line (left) and the WR 313 NS CSEM line (right) for the Vulcan data (top), 6.5 Hz OBEM data (middle) and 0.5 Hz OBEM data (bottom).

Figure 19 contains a map view of the Walker Ridge 313 survey area with geologic annotations after Hutchinson et al. (2008) and pseudosections for a frequency of 0.5 Hz. Pseudosections for Vulcan and 0.5 Hz and 6.5 Hz OBEM data are shown in Figure 20 for the EW and NS tows. The 6.5 Hz data has a much shallower depth sensitivity than the 0.5 Hz data, and exhibits relatively little resistivity structure. The salt wall in the south and east is evident in the

0.5 Hz pseudosections as a resistor that extends downwards beneath sites 9 and 14; the fact that it is barely present in the 6.5 Hz is an indication that it has a deep depth extent. Hydrates were found in both wells in the top of the seismic section as stratal-bound facture-filling gas hydrate and also within the dipping sheeted sands (horizons blue, orange, and green) deposits that occur deeper in the well (Boswell et al., 2009a). The pseudosections give resistive features under both 'G' and 'H' wells which could correspond with the JIP LWD resistivities. The pseudosections may be capturing the dipping strata, but further analysis is required before this can be quantified. The Vulcan pseudosections and OBEM pseudosections at WR 313 give a consistent story with resistivies that are similar in value and similar in structure and crossing pseudosections tie together well.
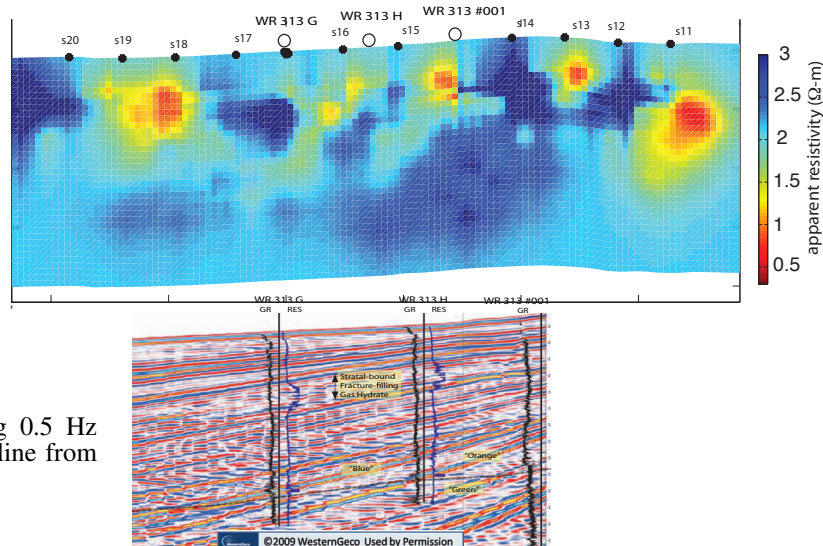

Figure 21: WR 313 EW-trending 0.5 Hz OBEM pseudosection and seismic line from Boswell et al. (2009a).

A closer look at the 0.5 Hz EW trending pseudosection is shown in Figure 21 with a corresponding EW seismic line from Boswell et al. (2009a). The JIP drilled two holes at WR313, 'G' and 'H', which are intersected by the EW CSEM line. Hydrates were found in both wells in the top of the seismic section as stratal-bound facture-filling gas hydrate and also within sheeted sands (Boswell et al., 2009a). The pseudosections give resistive features under both 'G' and 'H' wells, which could correspond with the JIP LWD resistivities. The pseudosections are perhaps capturing the dipping strata as shown in the seismic transect, but further analysis is required before this can be quantified.

Mississippi Canyon 118. This block had been designated as a Minerals Management Services observatory. Large outcrops of hydrate occur on the seafloor in relatively shallow water depths of 800-900 m, but there is yet no direct evidence of hydrate at depth. This area provides the opportunity to coordinate and collaborate with many other ongoing scientific programs, including shallow resistivity surveying. We deployed 24 receivers in a 6 x 4 array and towed 10 transmitter lines in a grid pattern (avoiding the already installed seafloor equipment with the OBEM deployments) (Figure 22).

Vulcan pseudosections for MC 118 are shown in Figure 23, and OBEM pseudosections are shown in Figure 24. MC 118 is conductive with a background resistivity of 0.5-1 Ωm and is generally featureless except at the SE crater. No constraints were placed on the intercepting tow lines and so the fact that three lines independently give a resistive body at the SE crater assures us that this is an attribute of the data due to geology. The EW line that crosses through the SE crater is overlayed on chirp acoustic line 119 from Sleeper et al. (2006) in order to compare acoustic blanking to electrical conductivity. The acoustic blanking or wipeout zones at MC 118 are attributed to authogenic carbonate as well as free gas and gas hydrate (Lapham et al. 2008). Carbonate rocks are present on the crater floors and have been noted in the SW crater (McGee et al. 2009 and 2008). The SE crater has a pavement of dead methanotrophic clams and there is no evidence for recent venting, which suggests that the conduit which once supplied methane to these clams became blocked, perhaps due to hydrate formation (McGee et al. 2009 and 2008). We find that the SE crater resistor appears to have some depth extent and the acoustic blanking there is associated with resistive structures. However, the acoustic blanking towards the SW crater (attributed to the shallow carbonates present there (Macelloni, pers comm.))
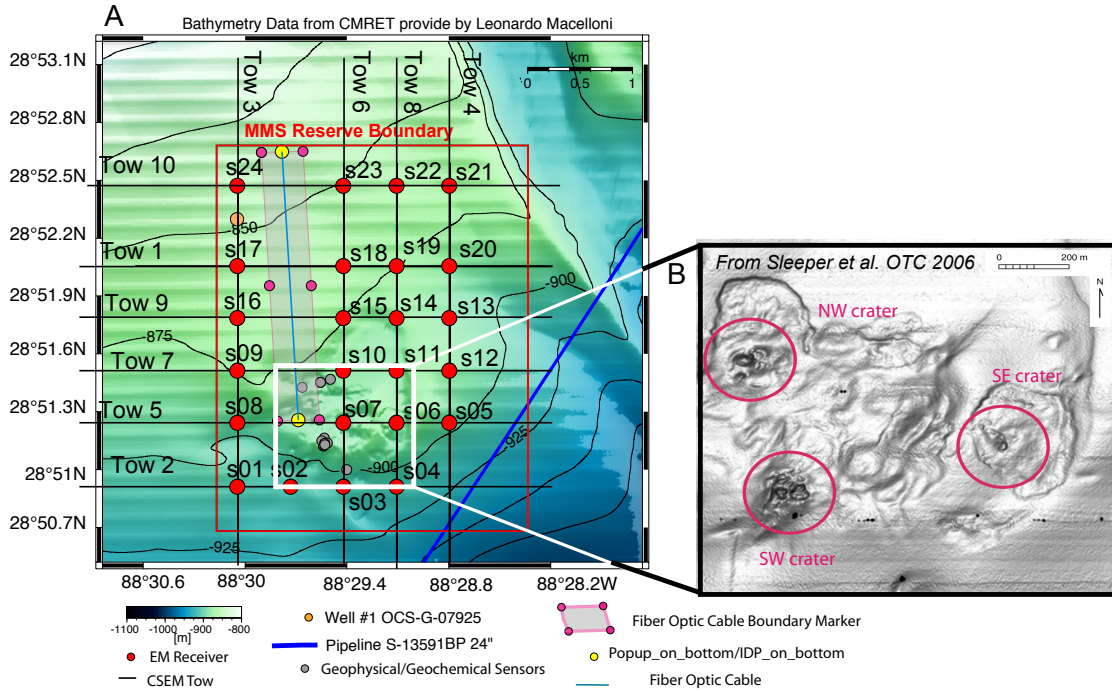
Figure 22: Survey map of Mississippi Canyon 118 with detail of the three crater complexes (bathymetry was provided by Leonardo Macelloni and the close up of the three crater complexes is from Sleeper et al., 2006).
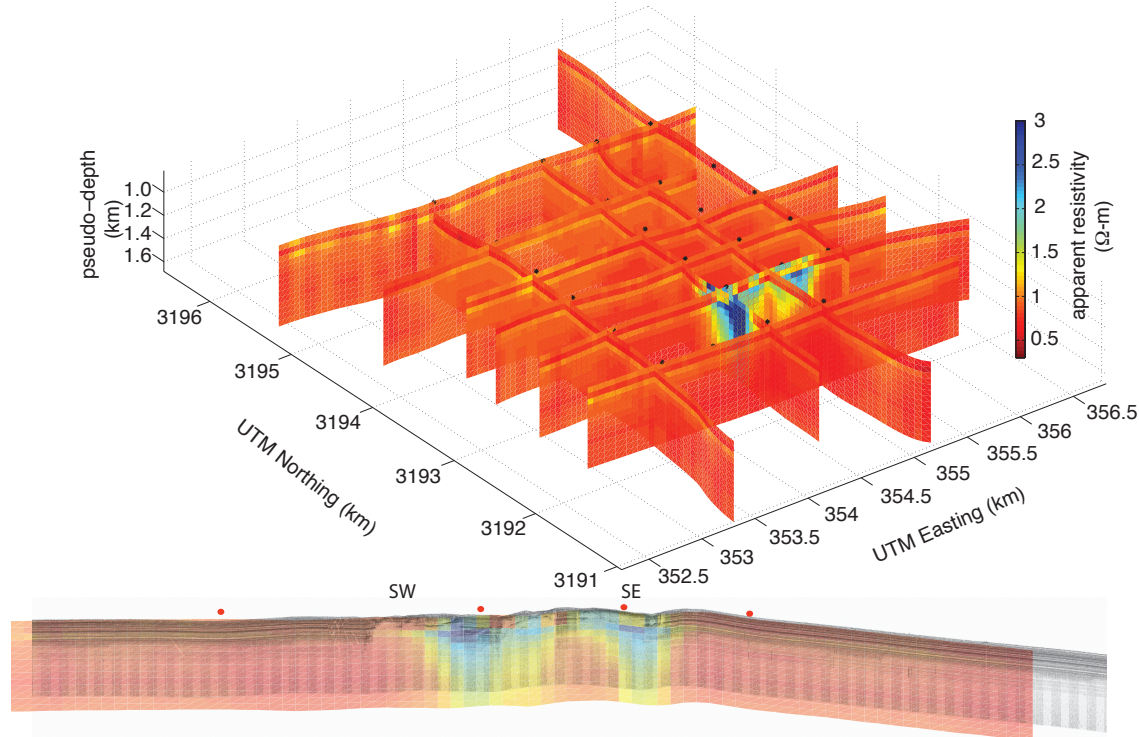
is associated with the background resistivity of 1 Ωm. This is significant, in that hydrate and carbonates, thought to be a confounding electrical resistors, are in fact differentiable here. Only drilling at the SE crater will confirm the presence of hydrate at depth.
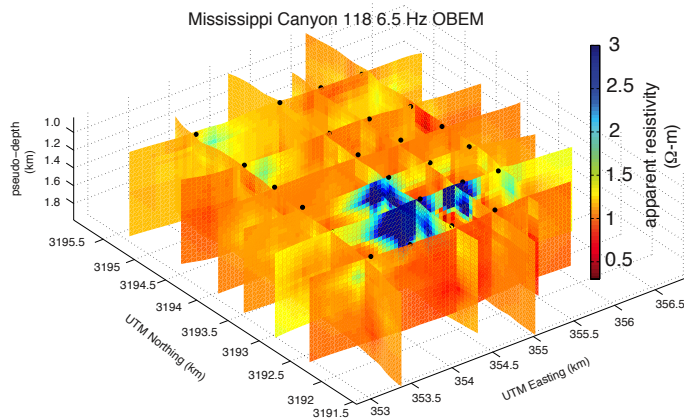
Figure 24: Mississippi Canyon 118 OBEM apparent resistivity pseudosections.

The OBEM pseudosections for 6.5 Hz are shown in Figure 24 and shows results consistent with the Vulcan pseudosections. Three CSEM tow lines independently give a resistor at the SE crater with a background resistivity of about 1 Ω-m. The seafloor receiver data images the top few kilometers of sediment and the Vulcan data images the top 100's of meters, and so seafloor background resistivities are slightly elevated in the OBEM data because they are sampling a larger sediment volume.

Figure 23: Apparent resistivity depth section based on frequency for Vulcan data collected at MC 118 and an EW transect from Line 5 overlayed on chirp acoustic data from Sleeper et al. (2006) which crosses the SE crater.

5. ESTIMATING HYDRATE VOLUMES FROM RESISTIVITY

While the apparent resistivity pseudosections provide a useful and compact way of looking at the data, and can provide some insight as to geological structure, the ultimate goal of our CSEM studies is to make quantitative inferences about hydrate saturation from resistivity estimates. For this, ideally we need to replace the apparent resistivities with resistivity estimated from inversion of the data. We had hoped that 1D inversion, which is computationally efficient and well understood, would prove useful for this purpose, as it still does for deep hydrocarbon mapping using CSEM methods. However, our pseudosection images indicated that the data are too complicated for application of 1D inversion, a problem that is exacerbated by significant bathymetry. We did experiment with 1D inversion of the MC 118 data, where the bathymetry is fairly flat and the background resistivity uniform, but the structure associated with inferred hydrate is still too three dimensional to obtain useful results. All the 2D and 3D CSEM inversion codes that existed during this work are proprietary to some degree or other. This not only makes access difficult, but also restricts our ability to make changes and optimizations to the code when we use it for novel applications such as hydrate imaging. However, Kerry Key of the Scripps EM group recently developed an efficient 2D CSEM inversion code, and it is our intention to use this code in the near future on the Gulf of Mexico data presented here, under separate funding. Meanwhile, we can illustrate the conversion of resistivity to hydrate volume using the MC 118 psedosection data, which will provide at least a lower bound on resistivity and hydrate fraction, and show the way to future work on these data sets.

Hydrate volume estimates may be made using Archie's Law and the Hashin-Shtrikman mixing laws. Archie's law is a heuristic relationship which works well for clastic sediment porosity, and is often used to convert resistivity from well logs to hydrate concentrations. The Hashin-Shtrikman bounds are extreme end-member cases which would be appropriate to model maximally disconnected hydrate (granules in the pore space) and maximally connected hydrate (hydrate filled fractures and veins).

Archie's Law is defined as:

$$\rho_t = a\phi^{-m}\rho_w/S_w{}^n \tag{1}$$

where a is the tortuosity factor, m is the cementation exponent of the rock, n is the saturation exponent, ϕ is the porosity, ρ_w is the resistivity of the pore fluid, S_w is the fluid saturation, and ρ_t is the measured resistivity (Archie 1942). We set $m = 2$, $n = 2$, and $a = 1$ for our computations. We can use Archie's Law to estimate the porosity of the sediment as a function of depth, by assuming the sediment is fully saturated with water (S_w= 1) (Ellis et al, 2008). This simplifies equation (1) to:

$$\rho_t = \phi^{-m}\rho_w(T, S) \tag{2}$$

where the pore fluid resistivity, $\rho_w(T, S)$, now varies as a function of temperature, T and salinity, S, based on the equation of state for seawater. The temperature as a function of depth can be predicted from seafloor temperature (4°C (Lapham, 2010)) and the geothermal gradient measured in the ARCO well at MC 118 of 17.2°C/km (Knapp et al. 2010). An estimate of the pore fluid conductivity at the seafloor is given from the transmitter's CTD sensors. Arps Law is then used to predict the fluid resistivity as a function of temperature (depth) (Collett and Ladd, 2000; Arp, 1953):

$$\rho_w(z) = \rho_w(0)(T(0) + 21.5°C)/(T(z) + 21.5°C) \tag{3}$$

where $z = 0$ is the surface of the seafloor. Finally, at MC 118 the background resistivity is about 1 Ω-m, and so we use this resistivity value for ρ_t. This further simplifies equation (2) and allows us to solve for porosity as a function of depth:

$$\phi = \rho_w(T, S)^{1/m} \tag{4}$$

Figure 25 shows the temperature, fluid resistivity and Archie predicted porosity-depth profiles.
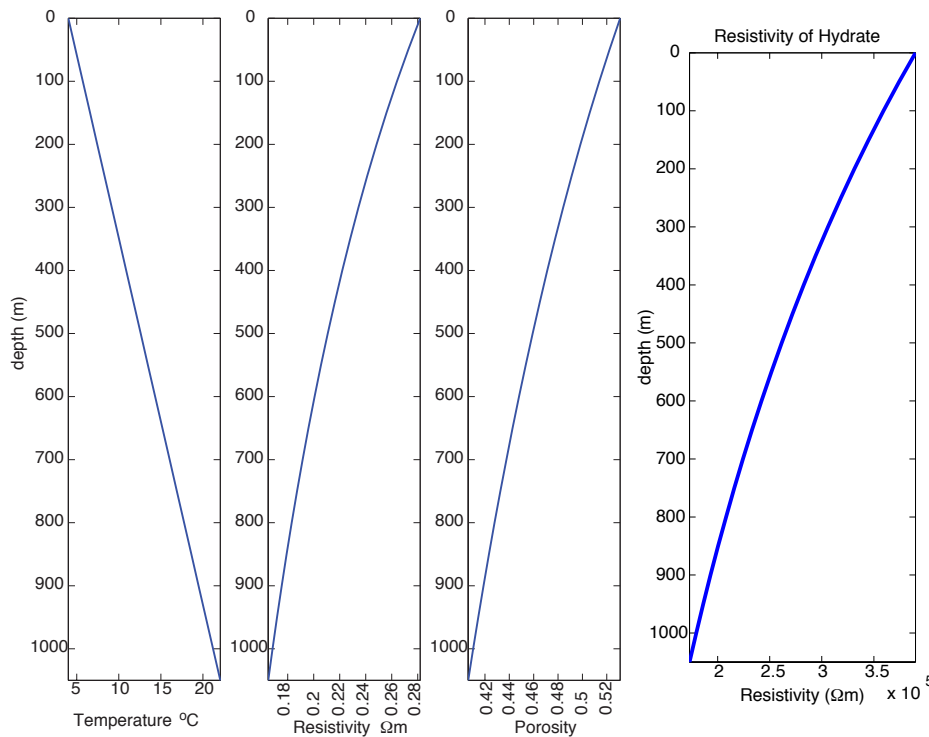
Figure 25. The temperature-depth profile, fluid resistance, and Archie predicted porosity-depth profile assuming a background resistivity of 1Ω-m. Also shown is hydrate resistivity as a function of depth/geothermal gradient based on the activation energy measured in the laboratory and presented earlier in this report.

Using the Archie calculated porosity for the region we can then rearrange equation 1 to solve for water saturation S_w:

$$S_w(z) = ((a\rho_w(z)\phi(z)^{-m}/\rho_t(z)))^{1/n} \tag{5}$$

where this time ρ_t represents our CSEM apparent resistivities as shown in Figure 24. Finally a hydrate saturation, S_h, can be computed:

$$S_h(z) = 1 - S_w(z). \tag{6}$$

This techinque is similar to that used by the ocean drilling program (Shipboard Scientific Party, 2003; Collett, 1998). Figure 26 (left) shows the hydrate volume estimates based on Archie's Law.

Another way to compute hydrate saturation is through the Hashin-Shtrikman binary mixing laws, which are the extremal bounds (HS-bounds) for effective conductivity, σ (Schmeling 1986; Hashin & Shtrikman 1963):

$$\sigma_{HS}^- = \sigma_s + (\beta)(1/(\sigma_f - \sigma_s) + (1-\beta)/(3\sigma_s))^{-1} \tag{7}$$

$$\sigma_{HS}^+ = \sigma_f + (1-\beta)(1/(\sigma_s - \sigma_f) + \beta/(3\sigma_f))^{-1}; \tag{8}$$

where β is the volumetric fraction of the fluid and σ_s and σ_f are the specific conductivities of the matrix solid and the fluid. The HS upper bound, σ_{HS}^+ corresponds to a connected fluid phase (conductive) with isolated solid phase (resistive) and the HS lower bound, σ_{HS}^-, corresponds to isolated spherical fluid inclusions (conductive) within a solid matrix (resistive) (Hashin & Shtrikman 1963). In terms of hydrate, the HS upper bound may represent a low concentration of granular disseminated hydrate distributed in isolated spheres within the conductive sediment. In clay-rich sediments hydrate may occur in veins or fractures and be better represented by the HS lower bound – where resistive material occurs in sheets impeding current flow through the matrix of fluid. Here we assume the water saturated sediments are the fluid phase, σ_f and that the hydrate is the solid phase, σ_s. We use the Arrhenius relationship and the constants from the laboratory conductivity measurements presented earlier in this report in order to compute a hydrate resistivity as a function of the geothermal gradient (Figure 25 right). The lower bound predicts resistivities that are higher than what we measure and so does not predict a useful hydrate volume. The upper bound which represents resistive inclusions within a conducting matrix does yield a sensible hydrate volume. The σ_{HS}^+, can be rewritten in terms of resistivity:

$$\rho_{HS}^+ = 1/\sigma_{HS}^+. \tag{9}$$

We compute σ_{HS}^+ values for a range of β values between 0 and 1 and then find the $\rho_{HS}^+(\beta)$ that best fits the CSEM apparent resistivities. We essentially create a look up table for resistivity and β. Figure 26 (right), shows the hydrate volume estimates predicted by the HS+ bound.
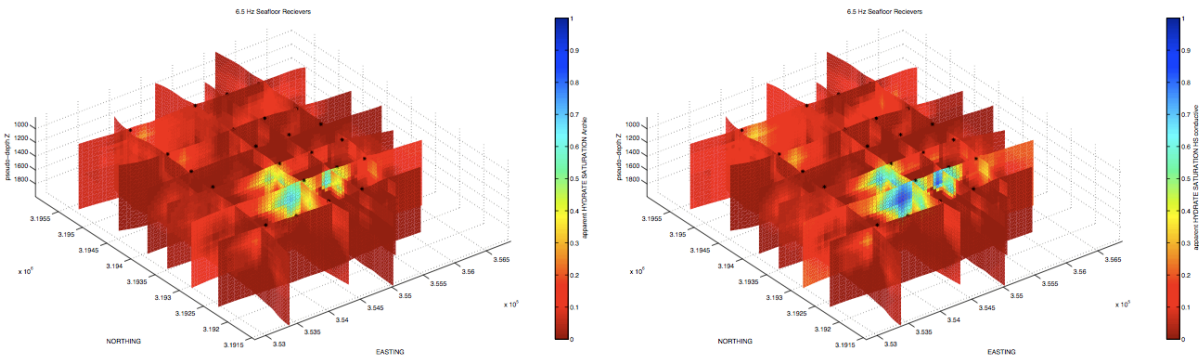
Figure 26: Apparent hydrate concentrations based on Archies Law (left) and the HS upper bound (right).

Archies Law lies between the HS upper and lower bounds and so the HS upper bound predictions of hydrate volume are slightly greater then those predicted by Archies Law. There is a general concentration of hydrate between 40 and 80% at the crater locations for MC 118. The remaining area is generally bland with very little hydrate predicted.

7. CONCLUSIONS

While much remains to be done in terms of the development of instrumentation and interpretation tools, we have made important progress in developing a comprehensive electromagnetic mapping method for imaging submarine gas hydrate. The ability to tow fixed-offset receivers above the seafloor reduces noise and allows operation in areas where sea-floor infrastructure would prevent the use of bottom-dragged systems. Our data show strong correlations with known geology, and excellent line to line repeatability. Our most compelling result comes from MC 118, where a strong, localized resistive feature has been clearly identified in the data over the SE crater, showing for the first time where sub-seafloor hydrate might exist at this location. The observation that authigenic carbonate does not necessarily express itself as a confounding resistor is also a very important result, providing more confidence that the resistive near-seafloor regions we observe are indeed representative of hydrates. While in many circumstances hydrate can be assumed to be simply very much more resistive than the host sediments, we have for the first time quantified the resistivity as a function of temperature of pure methane hydrate, and taken the first steps towards understanding multi-phase behavior of hydrate and sediment.

8. RESEARCH PRODUCTS

Technical transfer.

Matching funds for this project were provided by MMS, Chevron, ExxonMobil, WesternGeco, EMGS, Fugro, CGG/Veritas, Statoil, and Shell. Complete sets of the processed Gulf of Mexico CSEM data were delivered to these sponsors, and most sponsors were able to attend the annual Scripps Seafloor Electromagnetic Methods Consortium Sponsors Workshops held in March each year.

The work has excited broad industry interest, and we have ongoing projects funded by Fugro and Shell to continue the development and commercialization of the Vulcan towed systems.

Seminars, conference presentations, etc.

Lawrence Livermore National Laboratory, California, March 2009.

Scripps Seafloor Electromagnetic Methods Consortium Sponsors Workshop, La Jolla, California, March 2009 (two presentations)

Australian National University, Canberra, Australia, June 2009.

MARELEC meeting, Stockholm, Sweden, July 2009.

Japanese Recent Advances in Exploration Geophysics Meeting, Kyoto, October 2009.

AGU fall meeting, December 2009.

DoE Atlanta Hydrate Meeting, January 2010.

Scripps Seafloor Electromagnetic Methods Consortium Sponsors Workshop, La Jolla, California, March 2010.

20th Electromagnetic Induction Workshop, Giza, Egypt September 2010.

Scripps Seafloor Electromagnetic Methods Consortium Sponsors Workshop, La Jolla, California, March 2011.

MARELEC meeting, La Jolla, California, June 2011.

7th International Conference on Gas Hydrates (ICGH7), July 2011 (two papers)

Norwegian Geological Survey, Trondheim, February 2012.

Scripps Seafloor Electromagnetic Methods Consortium Sponsors Workshop, La Jolla, California, March 2012.

Publications.

Du Frane, W.L., L.A. Stern, K.A. Weitemeyer, S. Constable, J.C. Pinkston, and J.J. Roberts, 2011a. Electrical properties of polycrystalline methane hydrate. *Geophysical Research Letters*, **38**, doi:10.1029/2011GL047243.

Du Frane, W.L., L.A. Stern, K.A. Weitemeyer, S. Constable, and J.J. Roberts, 2011b. Electrical properties of methane hydrate + sediment mixtures. *Fire in the Ice, DOE NETL newsletter*, **11(2)**, 10-13.

Weitemeyer, K., and S. Constable, 2009. Cruise report: Imaging gas hydrate in the Gulf of Mexico using marine electromagnetic methods. *Fire in the Ice, Methane Hydrate Newsletter, National Energy Technology Laboratory*, **Winter 2009**, 4–6.

Weitemeyer, K., G. Gao, S. Constable, and D. Alumbaugh, 2010. The practical application of 2D inversion to marine controlled-source electromagnetic sounding. *Geophysics*, **75**, F199–F211.

Weitemeyer, K., and S. Constable, 2010. Tests of a new marine EM survey method. *Fire in the Ice, Methane Hydrate Newsletter, National Energy Technology Laboratory*, **March 2010**, 13–17.

Weitemeyer, K., and S. Constable, 2010. Mapping shallow seafloor structure with marine CSEM, examples from the Gulf of Mexico gas hydrate experiment. *First Break*, **6 (28)**, 97-102.

Weitemeyer, K.A., S. Constable, S. and A.M. Trehu, 2011. A marine electromagnetic survey to detect gas hydrate at Hydrate Ridge, Oregon. *Geophysical Journal International* , **187**, 45-62.

REFERENCES CITED

Archie, G. E., 1942. The electrical resistivity log as an aid in determining some reservoir characteristics, Transactions of the American Institute of Mining and Metallurgical Engineers, 146, 54—62.

Arps, J., 1953. The effect of temperature on the density and electrical resistivity of sodium chloride solutions, Petroleum Transactions, AIME, 198, 327—330.

Boswell, R., Collett, T., Frye, M., McConnell, D., Shedd, W., Mrozewski, S., Guerin, G. and Cook, A. [2010] Gulf of Mexico Gas Hydrate Joint Industry Project Leg II: Technical Summary.
$http://www.netl.doe.gov/technologies/oil-gas/FutureSupply/MethaneHydrates/JIPLegII-IR/$

Collett, T., 1998. Well log evaluation of gas hydrate saturations, in SPWLA 39th Annual Logging Symposium, pp. 1—14.

Collett, T. S. & Ladd, J., 2000. Detection of gas hydrate with downhole logs and assessment of gas hydrate concentrations (saturations) and gas volumes on the Blake Ridge with electrical resistivity log data, Proceedings of the Ocean Drilling Program, Scientific Results, 164, 179—191.

Cook, A., G. Guerin, S. Mrozewski, T. Collett, R. Boswell. 2010. Gulf of Mexico Gas Hydrate Joint Industry Project Leg II: Walker Ridge 313 LWD Operations and Results.

Ellis, M., Evans, R., Hutchinson, D., Hart, P., Gardner, J., & Hagen, R., 2008. Electromagnetic surveying of seafloor mounds in the northern gulf of mexico, Marine and Petroleum Geology, 25, 960—968.

Hashin, Z. & Shtrikman, S., 1963. A variational approach to the theory of the elastic behaviour of multiphase materials, Journal of Mechanics of Physical Solids, 11, 127—140.

Key, K. [2009] 1D inversion of multicomponent, multifrequency marine CSEM data: Methodology and synthetic studies for resolving thin resistive layers. Geophysics, 74(2) F9-F20.

Knapp James H., Camelia C. Knapp, Leonardo Macelloni, Antonello Simonetti, and Carol Lutken Subsurface Structure and Stratigraphy of a Transient, Fault-Controlled Thermogenic Hydrate System at MC-118, Gulf of Mexico Search and Discovery Article #50356 (2010) Posted November 22, 2010 Adapted from an oral presentation at AAPG Annual Convention and Exhibition, New Orleans, Louisiana, USA, April 11-14, 2010

Lapham, LL., JP Chanton, R. Chapman, CS Martens, 2010. Methane under-saturated fluids in deep-sea sediments: Implications for gas hydrate stability and rates of dissolution. Earth and Planetary Science Letters 298 (2010) 275—285.

McConnell, D., Boswell, R., Collett, T., Frye, M., Shedd, W., Guerin, G., Cook, A., Mrozewski, S., Dufrene, R. and Godfriaux, P. [2010] Gulf of Mexico Gas Hydrate Industry Project Leg II: Green Canyon 955 Site Summary. http://www.netl.doe.gov/technologies/oil-gas/FutureSupply/MethaneHydrates/JIPLegII-IR/

McConnell, D., R. Boswell, T. Collett, M. Frye, W. Shedd, G. Guerin, A. Cook, S. Mrozewski, R. Dufrene, P. Godfriaux. 2010. Gulf of Mexico Gas Hydrate Joint Industry Project Leg II: Walker Ridge Site Summary.

Bowsell, R., T. Collett, D. McConnel, M. Frye, B. Shedd, S. Mrozewski, G. Guerin, A. Cook, P. Godfriaux, R. Dufrene, R. Roy and E, Jones. 2009a. Joint Industry Project Leg II Discovers Rich Gas Hydrate Accumulations in San Reservoirs in the Gulf of Mexico. in *Fire in the Ice* pages 1-5.

Bowell, R., D. Shelander, M. Lee, T. Latham, T. Collett, G. Guerin, G. Moridis, M. Reagan and D. Golderberg. 2009b. Occurrence of gas hydrate in Oligocene Frio sand: Alaminos Canyon Block 818: Northern Gulf of Mexico. *Marine and Petroleum Geology,* doi:10.1016/j.marpetgeo.2009.03.005.

Fiduk, J.C., P. Weimer, B.D. Trudgill, M. G. Rowan, P. E. Gale, R. L. Phair, B. E. Korn, G. R. Roberts, W. T. Gafford,

R. S. Lowe, and T. A. Queffelec. 1999. The perdido fold belt , northwestern deep Gulf of Mexico, Part 2: seismic stratigraphy and petroleum systems. *American Associated of Petroleum Geologists Bulletin.* V. 83. No. 4 (April 1999) P. 578-612.

Hutchinson D.R., D. Shelander, J. Dai, D. McConnell, W. Shedd, M. Frye, C. Ruppel, R. Boswell, E. Jones, T. Collett, K. Rose, B. Dugan, W. Wood, T. Latham. 2008. Site Selection for DOE/JIP Gas Hydrate drilling in the northern Gulf of Mexico. *Proceedings of the 6th International Conference on Gas Hydrates (ICGH 2008),* Vancouver, British Columbia, Canada July 6-10 2008.

Jones, E., T. Latham, D. McConnell, M. Frye, J. Hunt Jr., W. Shedd, D. Shelander, R. Boswell, K. Rose, C. Ruppel, D. Hutchinson, T. Collett, B. Dugan, W. Wood. 2008. Scientific Objectives of the Gulf of Mexico Gas Hydrate JIP Leg II Drilling.*Offshore Technology Conference* Paper No. 19501.

Key, K. 2009. 1D inversion of multicomponent, multifrequency marine CSEM data: Methodology and synthetic studies for resolving thin resistive layers. *Geophysics* Vol. 74. No. 2 (March-April 2009)

Laphan, L.L., J.P. CHanton, C.S. Martens, K. Sleeper and J.R. Woolsey. 2008. Mircobial activity in surficial sediments overlying acoustic wipeout zones at a Gulf of Mexico cold seep. *Geochemistry, Geophysics, and Geosystems* Vol. 9. No. 6 (4 June 2008) Q06001, doi:10.1029/2008GC001944 ISSN 1525-2027

Latham, T. and D. Shelander, R. Boswell, T. Collett, M. Lee. 2008. Subsurface Characterization of the hydrate bearing sediemnts near Alaminos Canyon 818. *Proceedings of the 6th International Conference on Gas Hydrates (ICGH 2008),* Vancouver, British Columbia, Canada July 6-10 2008.

McGee, T., J.R. Woolsey, L. Lapham, R. Kleinberg, L. Macelloni, B. Battista, C. Knapp, S. Caruso, V. Goebel, R. Chapman, P. Gerstoft. 2008. Structure of a carbonate/hydrate mound in the northern Gulf of Mexico. *Proceedings of the 6th International Conference on Gas Hydrates (ICGH 2008),*Vancouver, British Columbia, Canada July 6-10 2008.

McGee, T., J.R. Woolsey, C. Lutken, L. Macelloni, L. Lapham, B. Battista, S. Caruso, V. Geobel. 2009. A multidisciplinary seafloor observatory in the northern Gulf of Mexico: results of preliminary studies. $http : //www.olemiss.edu/depts/mmri/programs/multidisciplinary.pdf$

Myer, D., S. Constable, and K. Key, 2011. Broad-band waveforms and robust processing for marine CSEM surveys. *Geophysical Journal International*, **184**, 689–698.

Shipboard Scientific Party, 2003. Proceedings ODP, Initial Reports, in Leg 204 Summary, vol. 204, chap. Leg 204 summary, pp. 1—75, eds Trehu, A. M., Bohrmann, G., Rack, F. R., Torres, M. E., & et al., Ocean Drilling Program, College Station TX.

Schmeling, H., 1986. Numerical models on the influence of partial melt on eleastic and anelastic and electrical properties of rocks. Part II: electrical conductivity, Physics of the Earth and Planetary Interiors, 43, 123—136.

Sleeper, K. A. Lowrie, A. Bosman, L. Macelloni, C.T. Swann. 2006. Bathymetric mapping and high resolution seismic profiling by AUV in MC 118 (Gulf of Mexico). *Offshore Technology Conference.* OTC-18133. May 1-4, 2006. data made available at: $http : //www.olemiss.edu/depts/mmri/programs/mc118/pro_map.html$

Smith, S., R. Boswell, T. Collett, M. Lee, and E. Jones. 2006. Alaminos Canyon Block 818: A documented example of gas hydrate saturated sand in the Gulf of Mexico. *Fire In the Ice* Fall 2006. Pages 12-13.

Stern, L. A., S. H. Kirby, S. Circone, and W. B. Durham (2004), Scanning electron microscopy investigations of laboratory?grown gas clathrate hydrates formed from melting ice, and comparison to natural hydrates, Am. Mineral., 89(8—9), 1162—1175.

National Energy Technology Laboratory

626 Cochrans Mill Road
P.O. Box 10940
Pittsburgh, PA 15236-0940

3610 Collins Ferry Road
P.O. Box 880
Morgantown, WV 26507-0880

One West Third Street, Suite 1400
Tulsa, OK 74103-3519

1450 Queen Avenue SW
Albany, OR 97321-2198

2175 University Ave. South
Suite 201
Fairbanks, AK 99709

Visit the NETL website at:
www.netl.doe.gov

Customer Service:
1-800-553-7681